https://doi.org/10.1016/j.compstruct.2022.116388

Intermediate crack-induced debonding in CFRP-retrofitted notched steel beams at different service temperatures: Experimental test and finite element modeling

Dong Guo[a], Wan-Yang Gao[b,c*], Yun-Lin Liu[d,e] and Jian-Guo Dai[a*]

[a] Department of Civil and Environmental Engineering, The Hong Kong Polytechnic University, Hong Kong 999077, China.

[b] Shanghai Key Laboratory for Digital Maintenance of Buildings and Infrastructure, School of Naval Architecture, Ocean and Civil Engineering, Shanghai Jiao Tong University, Shanghai 200240, China.

[c] State Key Laboratory of Ocean Engineering, Shanghai Jiao Tong University, Shanghai 200240, China.

[d] School of Civil Engineering, Anhui Jianzhu University, Hefei 230031, China.

[e] Prefabricated Building Research Institute of Anhui Province, Hefei 230031, China.

*Corresponding authors: wanyanggao@sjtu.edu.cn (W.-Y. Gao), cejgdai@polyu.edu.hk (J.-G. Dai)

Abstract: Carbon fiber-reinforced polymer (CFRP)-retrofitted steel beams are likely exposed to significant service temperature variations due to seasonal and daily temperature changes. However, there is lacking research on the structural performance of CFRP-retrofitted steel beams under service temperature variations. This paper presents an experimental study of fourteen beams including one intact beam, one notched beam and twelve CFRP-retrofitted notched beams tested at various service temperatures from -20°C to 80°C. The structural properties including load-deflection curves, load capacities at initial and ultimate debonding, crack mouth opening displacements at the notch and the CFRP strain measurements were examined and compared at different service temperatures. The debonding loads of CFRP-retrofitted beams were increased with the temperatures from -20°C to 60°C and decreased at 80°C. A formula was proposed to derive the local bond-slip behavior of the CFRP-to-steel interface at different temperatures from the CFRP strain measurements. The shear stiffness of the interface generally decreased with the service temperature growth, while the interfacial fracture energy first increased and then decreased. A finite element model was proposed to gain insight into the effects of interfacial thermal stress and temperature-dependent bond properties on the bond behavior and structural performance of CFRP-retrofitted beams at different service temperatures.

Keywords: Steel beam, CFRP strengthening, temperature variation, debonding, thermal effect, bond-slip behavior.

1. Introduction

Externally bonded carbon fiber-reinforced polymer (CFRP) plates are widely used for the strengthening of steel structures. Existing studies have demonstrated the effectiveness of the CFRP strengthening technique in enhancing the structural performance of steel beams with initial cracks (notches) under static [1-4] and fatigue loadings. For example, Deng *et al.* [2] reported that the load-carrying capacity of the notched steel beam under static loading could be doubled by CFRP retrofitting. The effects of loading scheme, FRP thickness, bonding adhesive and anchorage system on the fatigue performance of CFRP-retrofitted steel beams were investigated by Chen *et al.* [5], Yu *et al.* [6,7] and Colombi *et al.* [8]. Deng *et al.* [9] compared the fatigue properties of CFRP-retrofitted steel beams with externally bonded CFRP plates with different prestress levels. Wang *et al.* [10] studied the bond behavior of CFRP-to-steel strap joints under overloading fatigue and wetting/drying cycles. In addition, the CFRP strengthening can significantly delay crack propagation under fatigue loading, thereby prolonging the fatigue life of cracked or deficient steel beams [11]. The bonded CFRP plate bridges both sides of the crack and effectively restraints the crack opening. However, the high tensile force sustained by the CFRP plate at the crack locations also generates high stress concentrations at the bond interface between the CFRP plate and the steel beam, which may lead to the occurrence of interfacial debonding. According to the existing experimental observations, such interfacial debonding usually starts at the cracked part, and thus it is termed as intermediate crack-induced (IC) debonding. The IC debonding limits the full utilization of the high strength of CFRP plates and the enhancements of the load-carrying and deformation capacities of the strengthened steel beams. Therefore, the bond action between the CFRP plate and the steel substrate is of vital importance in governing the performance of the CFRP-retrofitted cracked steel beams. The bond behavior of the CFRP plate-to-steel interface is usually determined by the pull-out tests of CFRP-to-steel bonded joints [12-23]. As the most fundamental law describing the interfacial bond behavior, several types of local bond-slip models have been proposed, including elastic-brittle [24,25], elastic-plastic-brittle [26,27], trapezoidal (i.e., elastic-constant stress-softening) [28-32] and bilinear (i.e., elastic-softening) types [29,30]. The proposed bond-slip models are also widely used in analytical solutions for predicting the plate-end debonding failure of FRP-retrofitted steel beams [27,33], the IC debonding failure of FRP-retrofitted notched steel beams [2], and the deformation process of FRP-to-concrete/steel bonded joints [34-37]. In addition, finite element (FE) modeling has been employed to predict the structural performance of FRP-strengthened structures by considering the interfacial bond-slip models [11,28,38-40].

On the other hand, the performance of CFRP-retrofitted steel beams may be significantly affected by temperature variations in service. This is because the properties of adhesive layers usually formed from epoxy resins may change at different service temperatures, especially when the temperature is close to or above the glass transition temperature (T_g) [15,20,21,41-43]. The reported T_g values of most commercial epoxy resins used for structural bonding are around 40~65°C [21,44], and this temperature range can be reached when steel structures are directly exposed to sunlight [27,45]. In addition to the temperature-induced deterioration of the bonding adhesive, thermal stresses may be generated at the interface as the service temperature varies. This is because as the service temperature increases/decreases, the thermal expansion/extraction of the steel substrate is much higher than that of the bonded CFRP plate because of the larger coefficient of thermal expansion (CTE) of steel than that of CFRP along the longitudinal fiber direction. As a result, large thermally-induced stresses/slips can occur at the interface between the CFRP plate and steel [35,46-49]. Such interfacial thermal stresses/slips are possibly in the same or opposite direction as those generated by mechanical loading, which may accelerate or delay the debonding propagation and consequently lead to a reduction or increase in the debonding load of the strengthened beam.

Some research groups including the authors have conducted theoretical analyses to investigate the effects of interfacial thermal stresses on the full-range deformation behavior of FRP-to-steel bonded joints and to predict the debonding loads with due consideration of the thermal stress effects [46-51]. By isolating the effects of thermal stresses, the interfacial bond behavior (i.e., the local bond-slip relationship) between the CFRP plate and steel substrate can be derived based on the measured strains of the CFRP plate. It has been found that the bond-slip relationship, including interfacial shear stiffness, peak shear stress and interfacial fracture energy, is significantly influenced by relatively high temperatures [15,18,37,41]. Based on the measured bond-slip relationships (i.e., test data), Biscaia *et al.* [15] proposed a bilinear bond-slip model between the CFRP plate and the steel substrate by using temperature-dependent bond parameters (i.e., interfacial fracture energy, shear stiffness, etc.). Recently, the authors also developed an analytical solution to describe the effects of thermal stresses on the IC debonding process of CFRP-retrofitted steel beams [48]. It was found that the thermal stresses induced by high service temperatures tended to alleviate the stress concentrations near the notch section and thus improved the debonding load, and vice versa. The proposed analytical solution was validated through comparison with the finite element (FE) analysis results instead of test data. The above literature review has indicated that the current research about the effect

of thermal loading on the IC debonding failure of FRP-retrofitted steel beams is based on the analytical and FE studies, while the experimental results are not available.

This study aims to fill the current research gap and presents the results of a comprehensive experimental study that extensively investigates the effects of different service temperatures on the structural performance of CFRP-retrofitted notched steel beams. Such test results also serve as a benchmark for the validation of the FE model, which aims to gain insight into the temperature effects on the IC debonding mechanism of CFRP-retrofitted notched steel beams at different service temperatures.

2. Experimental Program

2.1. Specimens

The experimental program consisted of flexural bending tests on twelve CFRP-retrofitted notched steel beams at various temperatures, including -20°C, 0°C, 30°C, 45°C, 60°C and 80°C. **Fig. 1** shows the configuration of the tested specimens. The design of the specimens is similar to that used in the experimental study conducted by Deng *et al.* [2] at normal temperature. Considering that the "effective bond length" of the CFRP strengthening system may be increased at high temperatures [18,47,52], the length of the CFRP plate was changed from 400 mm in Deng *et al.*'s study [2] to 800 mm in the current experimental program.

As shown in **Fig. 1**, the CFRP-retrofitted steel beams were tested under four-point bending. The beams were supported by two roller supports at a clear span of 1.1 m and loaded by a load distributor with a constant moment zone of 0.2 m. The total length of the steel beams was 1.3m. The steel beams were prefabricated with a notch to simulate the crack defect on the soffit of the steel beam. Each retrofitted steel beam was strengthened by a 0.8 m long CFRP plate. In addition, two different thicknesses (1.2 mm and 1.4 mm) of CFRP plates were used for the strengthening applications. The specimens were named according to the CFRP plate thickness and the tested service temperature. For example, "BnP1.4T30" represents the notched steel beam retrofitted by a 1.4 mm thick CFRP plate and tested under 30°C. In addition, the notched steel beam without retrofitting (Bn) was also tested as a reference. The details of all the specimens are summarized in **Table 1**.

The close view of the prefabricated notch is shown in **Fig. 1c**. The width of the crack opening is 5 mm and the height of the opening is the same as the thickness of the bottom flange. In addition, a narrow notch was cut in the web, which was perpendicular to the longitudinal axis of the beam and had a width of 0.18 mm and a height of 8 mm. In addition, some plate

stiffeners with a thickness of 6 mm were welded on both sides of the beam web at the loading and supporting points to avoid local buckling.

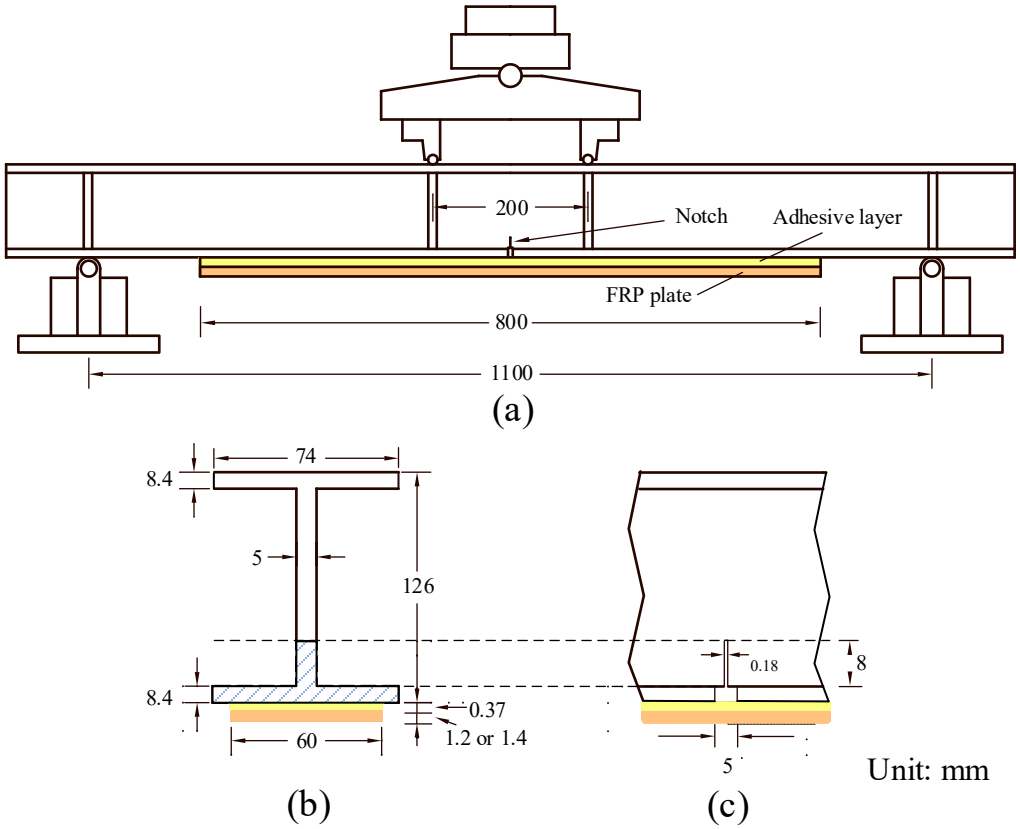

Fig. 1 Schematic of the CFRP-retrofitted steel beam: a) front view; b) side view; c) close view of the precast notch.

Table 1 Detail of the specimens

Specimen name		CFRP plate thickness (mm)	Tested temperature (°C)
Bn		-	30
BnP1.2	BnP1.2T-20	1.2	-20
	BnP1.2T0		0
	BnP1.2T30		30
	BnP1.2T45		45
	BnP1.2T60		60
	BnP1.2T80		80
BnP1.4	BnP1.4T-20	1.4	-20
	BnP1.4T0		0
	BnP1.4T30		30
	BnP1.4T45		45
	BnP1.4T60		60
	BnP1.4T80		80

2.2. Materials

The properties of the steel were measured according to ASTM A370 [53]. The elastic modulus, yield strength and Poisson's ratio were 210.5 GPa, 359 MPa and 0.27, respectively. The properties of the CFRP plates, measured according to ASTM D3039 [54], were given by the manufacturer. The elastic moduli of the 1.2 mm and 1.4 mm thick CFRP plates were 171.3 GPa and 158.2 GPa, and the corresponding tensile strengths were 2743.3 MPa and 3044.4 MPa, respectively. In addition, the coefficients of thermal expansion (CTEs) of the materials were measured by thermomechanical analysis (TMA) test according to BS ISO 11359 [55]. The measured CTEs of steel, 1.2 mm and 1.4 mm CFRP plates were 1.14×10^{-5}/°C, -9.10×10^{-7}/°C and -8.48×10^{-7}/°C, respectively.

Sikadur-330CN was used as the adhesive for bonding the CFRP plate onto the steel beam. The mechanical properties of the bonding adhesive at room temperature, including the tensile strength and the elastic modulus were 49.7 MPa and 2.55 GPa, respectively, as provided by the manufacturer. Moreover, the thermal degradation of the bonding adhesive, which was prepared and cured in the same environments as the beam specimens, was measured by the dynamic mechanical analysis (DMA) according to ASTM D7028 [56]. The DMA test was performed on a single cantilever configuration with a heating rate of 2°C/min and an oscillation frequency of 1 Hz. **Fig. 2** shows the measured changes in storage (elastic) modulus, loss (viscous) modulus and tan delta (i.e., the ratio of loss modulus to storage modulus) with the temperature growth. The storage modulus is a measure of the elastic response of a material but not the same as Young's modulus [56]. The previous study demonstrated that the temperature-dependent storage modulus was in significant correlation with the elastic modulus determined through traditional mechanical tests (i.e., tensile or flexural tests) [57]. It can be observed that as the temeprature increases, the elastic modulus decreases slightly at relatively low temperatures and then drops sharply in the glass transition region. According to different definitions of T_g [56], the T_g is 56.25°C at the onset of softening, 60.15°C at peak loss modulus and 69.74°C at peak tan delta.

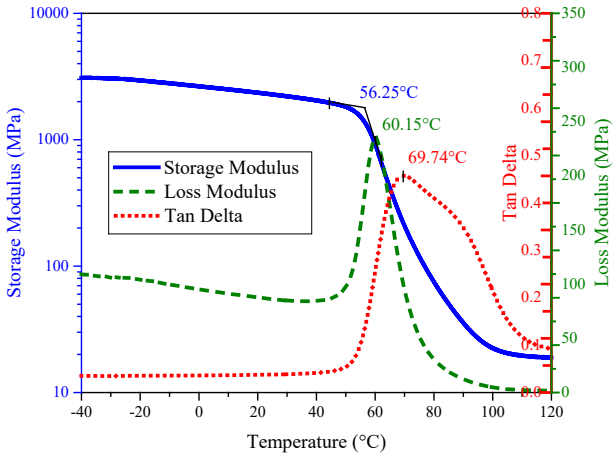

Fig. 2 DMA results

2.3. Strengthening application

The bottom surface of each steel beam was degreased with acetone and sandblasted to remove the oxide coating (**Fig. 3)**. A 0.25 mm diameter angular alumina grit was used for the sandblasting of the bottom surface of each steel beam to ensure its chemical compatibility with the adhesive, following the suggestions provided by Fernando *et al.* [58]. In addition, the blasting angle was controlled at about 75° [59], and the pressure was controlled within 0.4-0.6 MPa. After sandblasting, the steel surface was cleaned away from any dust with compressed air. Before bonding to the steel surface, the CFRP plate was carefully cleaned with acetone using gauze. Afterwards, the CFRP plate was adhesively bonded to the steel beam within half an hour, avoiding the oxidation of the steel surface. As Deng and Lee [60] recommended, more adhesives were laid along the center than the outer edges, which allowed the air trapped between the adherends to escape when they were pushed together. Then constant compressive stress of 4.2 kPa was applied on the top surface of the CFRP plate to ensure that the externally bonded CFRP plate and the steel beam were tightly bonded together during the curing process of the CFRP strengthening system [38,61]. Afterwards, to avoid spew fillet and estimate the consumption of epoxy resin, the excess adhesive along the sides of the plate was scraped off, collected and weighted. The average epoxy resin weight for each specimen was 22.8 g. Therefore, the average thickness was about 0.37 mm. The CFRP-retrofitted steel beams were cured at room temperature for about six months before the bending tests.

Fig. 3 Sandblasting of the steel surface

2.4. Testing procedure and instrumentations

The following testing procedure was used: first, the beam was placed in the environmental chamber and the internal temperature was changed; second, after the target temperature was reached, it was maintained at a nearly constant value. Finally, the beam was mechanically loaded until failure.

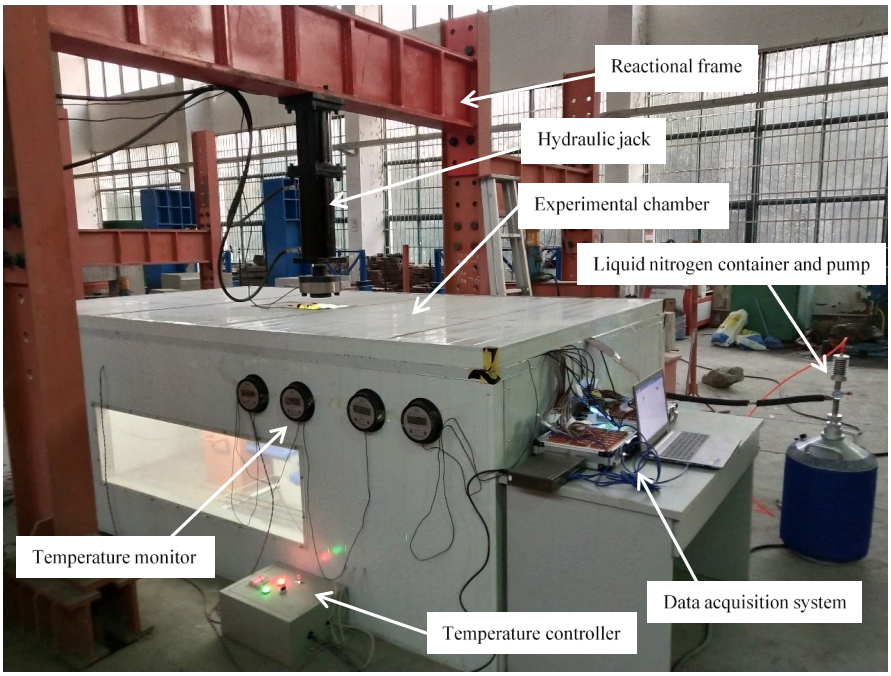

Fig. 4 The environmental chamber

As shown in **Fig. 4**, an environmental chamber with size of 3.4 m × 1.9 m × 1.2 m was built with heating insulation boards to reduce possible heat exchange between the specimens and the out-chamber air during the tests. A heating and cooling system was specifically designed to adjust the temperature in the chamber. The chamber was heated by electronic heating pipes while cooled down by liquid nitrogen pumping. An electric fan was installed to help reduce temperature gradients inside the chamber and achieve an even temperature

environment. In order to monitor the temperature variations of the beam specimen, four K-type thermocouples were installed at different locations on the specimen surface, including the CFRP plate surface, the beam web at the mid-span location, and the upper flange of the steel beam at both ends. **Fig. 5** shows the change of temperatures measured at different locations of the specimen under the 60°C testing temperature. It can be seen that the measured temperatures were quite close to each other at various locations and changed gradually according to the set temperature. Similar temperature changing schemes were employed for the heating/cooling process of the specimens tested at other service temperatures (i.e., -20°C, 0°C, 30°C, 45°C and 80°C). Note that the heating/cooling process was divided into several small steps with temperature intervals of 15 or 20°C. After the measured temperature of the specimen reached the target value, the air temperature inside the chamber was maintained at an almost constant value for at least 30 minutes to ensure that the temperatures of the specimen measured at different locations were almost the same.

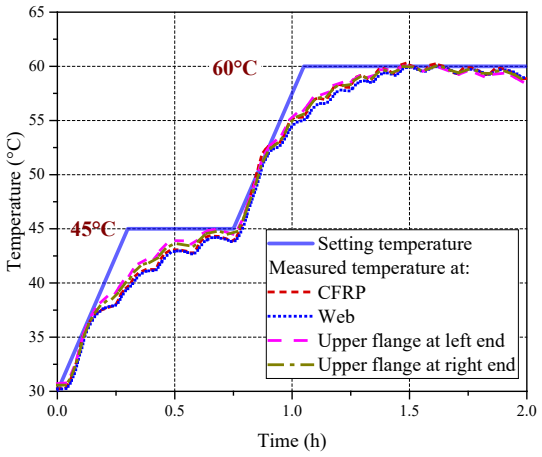

Fig. 5 Measured temperature history of the specimen during the heating process

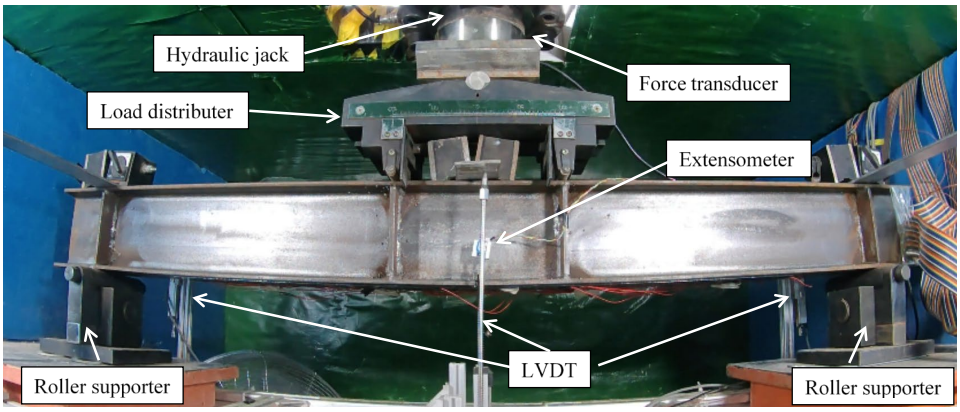

Fig. 6 Experimental setup inside the environmental chamber

Fig. 6 shows the loading and measurement apparatus. The mechanical loading was applied by an electro-hydraulic loading and control system at a constant loading speed of 3 mm/min.

Moreover, the two supports and the loading points of the load distribution girder were designed with smooth rollers, which could rotate freely. This seemed to be important in previous experiments [62], but was often overlooked. During the loading process, the applied loads, mid-span deflections, axial strain distributions in the CFRP plate, and crack mouth open displacements (CMODs) at the notch location were recorded simultaneously by a computer-aided program at a frequency of 5 Hz. The mid-span deflection responses were obtained from the readings of six LVDTs located at the mid-span and both ends of the beam. The strain gauges were bonded to the CFRP surface using NP-50B adhesive, which could be used in temperatures ranging from -30°C to 300°C. Furthermore, for thermal compensation purpose, strain gauges from the same batch were attached to the TiS glass and placed near the strain measurement points [17]. Special considerations were given to the arrangement of strain gauges. The spacing of the strain gauges was set to 10 mm near the notch, where the values of the interfacial shear stresses are relatively high, 20 mm near the plate ends, and 30 mm between these two regions. In total, 44 strain gauges were used to measure the strain distributions along the CFRP plate (see **Fig. 7** for more details).

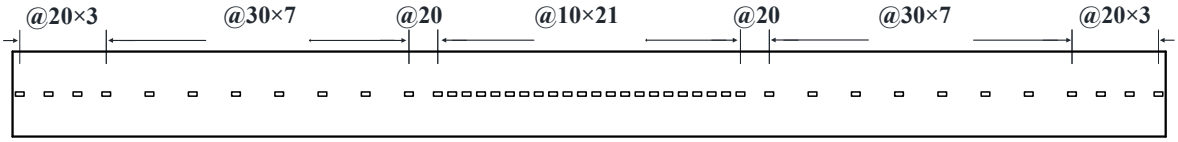

Fig. 7 Locations of strain gauges attached on the CFRP plate

The CMOD is also an important parameter to show the strengthening efficiency of CFRP plates [5,6]. As shown in **Fig. 8,** on each side of the beam an extensometer was installed at the two sides of the notch of the bottom flange to measure the CMOD. The extensometers used has a gauge length of 10 mm, a maximum deformation capacity of 4 mm and an accuracy of 0.012 mm.

To correct the eccentricity of the applied load and possible torsion of the beam during the loading process, the beam was pre-loaded to around 10 kN. Then the two measured CMODs were compared so that the loading apparatus could be adjusted if necessary.

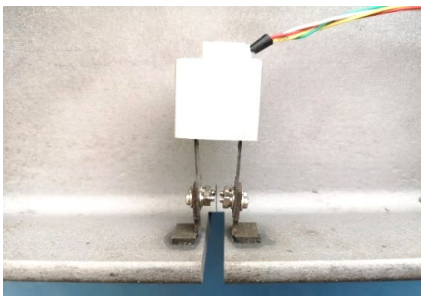

Fig. 8 The extensometer

3. Experimental Results

3.1. Test observations

Fig. 9a shows a typical failure mode of the CFRP-retrofitted steel beams. The typical failure of the retrofitted steel beams was due to interfacial debonding on one side. At the same time, the steel beam had a certain residual deformation after unloading. A local buckling of the steel beam was not found due to the presence of steel stiffeners. In addition, the propagation of the prefabricated crack tip was found in the retrofitted steel beams, mainly due to the continuous loading after the CFRP debonding. **Fig. 9b** shows a close-up view of the debonded side of the CFRP-retrofitted steel beam. After debonding, the CFRP plate had no residual deformation due to the material elasticity characteristics. **Fig. 9c&9d** show the close-up views of the debonded interface on both the CFRP plate and substrate steel sides. It is clearly seen that the cohesive failure, which occurs inside the adhesive layer, is the dominant failure mode.

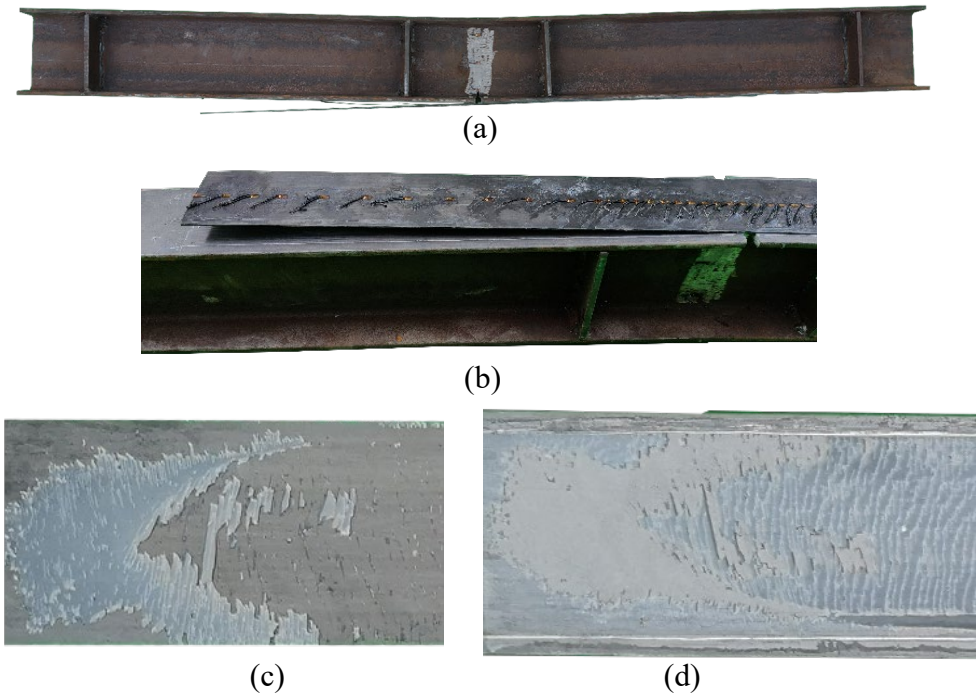

Fig. 9 Typical failure mode of the CFRP-retrofitted steel beams: a) front view; b) close-up view of the debonded side; and close-up views of the debonded surface c) on the CFRP plate; d) on the substrate steel side.

3.2. Structural performance of two CFRP-retrofitted steel beams tested at room temperature

Fig. 10 shows the load-deflection and the CMOD-load curves of two CFRP-retrofitted steel beams and the notched steel beam without retrofitting, which were tested at normal temperature (i.e., 30°C). It is seen that, under a low level of mechanical loading, the load-deflection curves exhibited typical elastic behavior and the deflections increased linearly with

the applied loads. For the notched beam without retrofitting, the flexural stiffnesses of the steel beam decreased after the steel yielding, and then exhibited almost plastic behavior with increasing CMOD values. In comparison, for the retrofitted steel beams, the initiation of interfacial debonding occurred at one side, which was witnessed by the reduced interfacial stress measured at this side to almost zero. The loads at the onset of debonding for both specimens were quite close (65.6 kN vs. 65.0 kN). Then the interfacial debonding propagated gradually from the notch to the plate ends with almost the constant axial force sustained by the CFRP plate at the notch location. Meanwhile, the flexural stiffness of the CFRP-retrofitted beam decreased slightly, while the steel beam remained elastic. After the steel yielded, the load increased at a much lower rate, accompanied by a rapid increase in the CMOD. Finally, the load dropped abruptly corresponding to the ultimate debonding.

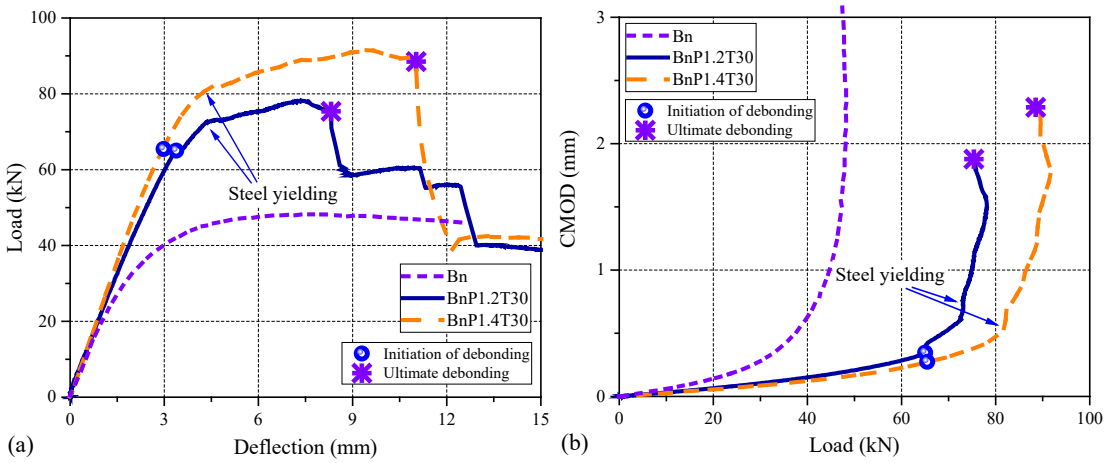

Fig. 10 Structural performance of two CFRP-retrofitted steel beams tested at room temperature: a) the load-deflection curves; b) the CMOD-load curves.

The strain distributions of the CFRP plate under different loading levels are shown in **Fig. 11**. At relatively low load levels, the strains in the CFRP plate increased from zero at the end of the CFRP plate to a maximum value at the notch. Moreover, the axial strain values at each location grew with the increasing load. As seen in **Fig. 11**, the axial strains along the bond length of the two specimens were distributed almost symmetrically around the notch at lower load levels (e.g., 20 kN, 40 kN and 60 kN). However, when the load was further increased, interfacial debonding initiated near the notched section at one side, where the axial strains in the CFRP plate remained almost unchanged, indicating the presence of an interfacial debonding zone there.

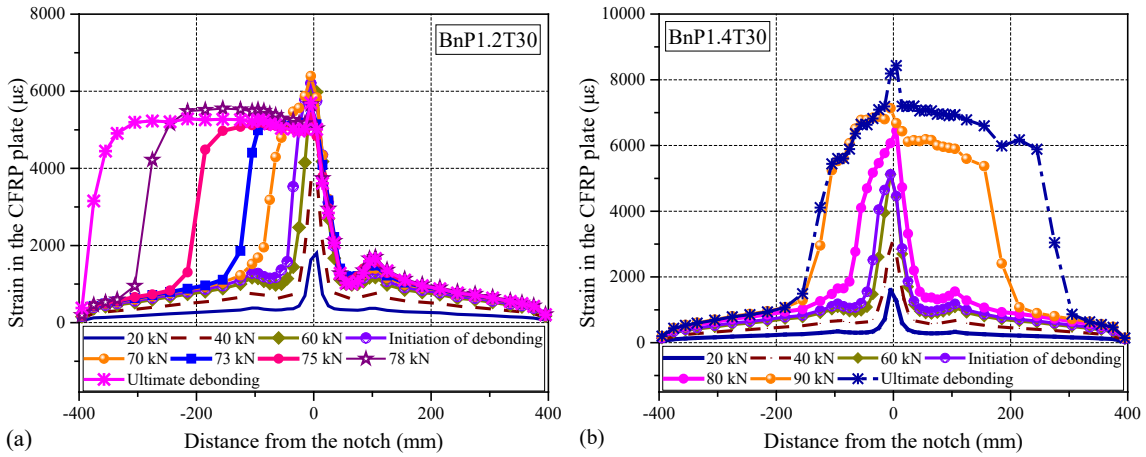

Fig. 11 Strain distributions in the CFRP plate: a) BnP1.2T30; b) BnP1.4T30.

Using the measured CFRP strains along the bond length, the local interfacial shear stress ($\tau_{i+\frac{1}{2}}$) (i starts from the plate end) between two subsequent strain gauges at the locations of x_i and x_{i+1} could be derived based on the difference of the measured strains (i.e., $\varepsilon_{i+1} - \varepsilon_i$) using the following equation [13,30,63]:

$$\tau_{i+\frac{1}{2}} = \frac{\varepsilon_{i+1}-\varepsilon_i}{x_{i+1}-x_i} E_f t_f \quad (1)$$

where E_f and t_f are the elastic modulus and the thickness of the CFRP plate, respectively.

Fig. 12 shows the distributions of the interfacial shear stresses in the two beams tested at 30°C. When the applied load was low, the entire bond interface was in the elastic (*E*) stage and the interfacial shear stresses were higher near the notch and plate ends. When the interfacial shear stress near the notch increased to the maximum value, the interface entered the elastic-softening (*E-S*) stage and the local interfacial shear stress started to decrease. With the further increase of the applied load, the interfacial shear stress near the notch decreased gradually to almost zero, indicating that the local interfacial debonding occurred. Then, during the elastic-softening-debonding (*E-S-D*) stage, the interfacial debonding propagated from the notched section to the plate end. The location corresponding to the maximum shear stress was then shifted from the notch to the plate end. With the propagation of the debonding failure, the deflections of the CFRP-retrofitted notched steel beams grew significantly accompanied by a slight increase of the applied load. Finally, as seen in **Fig. 10**, an abrupt drop of the applied load occurred due to the failure of the CFRP-retrofitted steel beams (i.e., complete debonding/separation of the CFRP plate from the beam typically over one span).

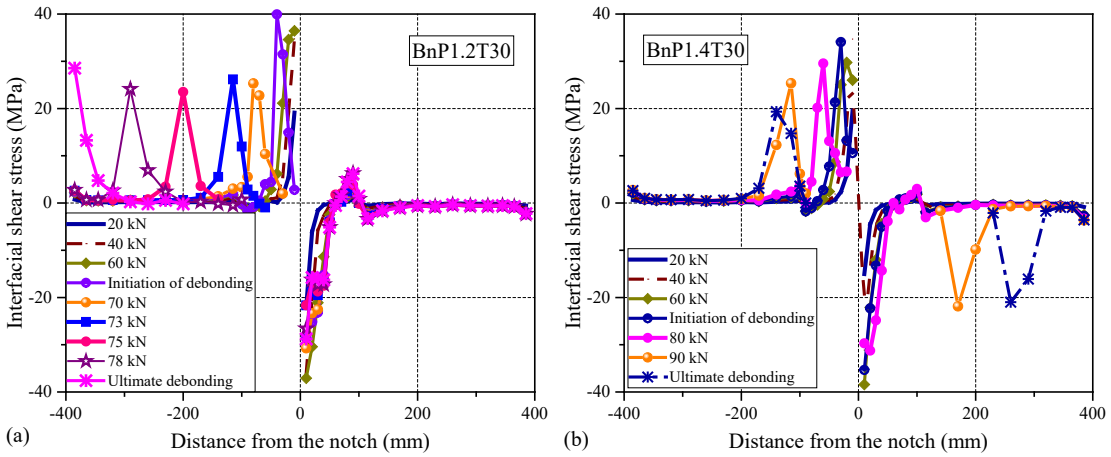

Fig. 12 Distributions of interfacial shear stresses: a) BnP1.2T30; b) BnP1.4T30.

3.3. Structural performance of CFRP-retrofitted steel beams tested at other temperatures

3.3.1. Load-deflection curves

Fig. 13 compares the load-deflection curves of the un-strengthened notched steel beam and the CFRP-retrofitted steel beams tested at different service temperatures. Due to the CFRP strengthening, the load-carrying capacities (i.e., the loads at the ultimate debonding) of the retrofitted beams were significantly enhanced. However, the measured curves of the CFRP-retrofitted steel beams were quite different at different temperatures. The highest load-carrying capacity and ultimate deflection were achieved at 60°C. In contrast, the load-carrying capacity and deformability of the CFRP-retrofitted steel beams were significantly reduced at low service temperatures (i.e., -20°C and 0°C). At 80°C, the load-carrying capacity of the retrofitted beams was also decreased due to the softening of the bonding adhesive. In addition, the residual strength of BnP1.4T-20 was smaller than that of the notched steel beam without retrofitting, which might be due to the abrupt propagation of the prefabricated notch along the beam depth observed during the debonding process of the externally bonded CFRP plate.

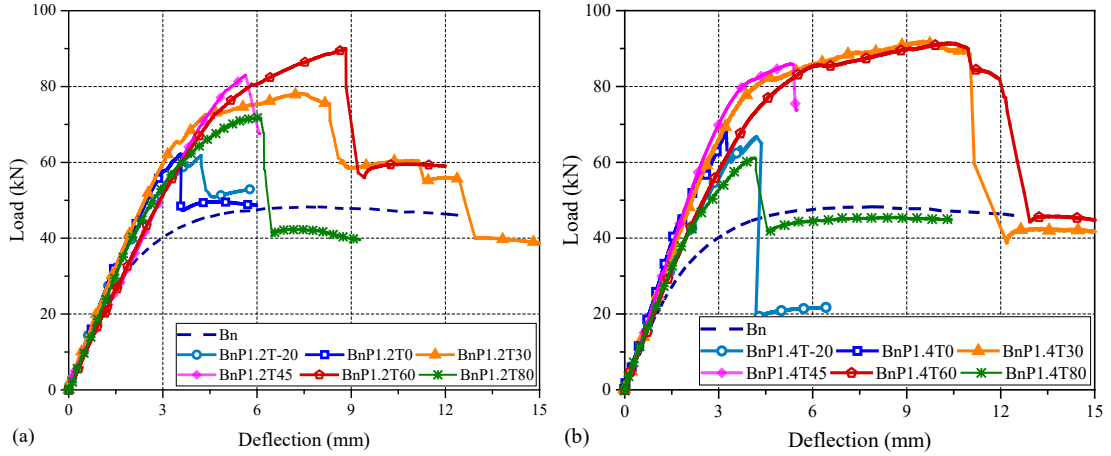

Fig. 13 Load-deflection curves of a) BnP1.2 and b) BnP1.4 at different service temperatures.

Table 2 summarizes the load capacities at the initial debonding and ultimate debonding of the CFRP-retrofitted steel beams at different temperatures. The maximum load-carrying capacity was achieved at the temperature range of 30°C to 60°C. The variations of the load capacities as the temperature changes are shown in **Fig. 14**. It is seen that the load capacities of CFRP-retrofitted steel beams were increased with the growth of the temperature when the temperature was lower than 60°C while reduced significantly at 80°C. In addition, the load-carrying capacities of the notched steel beams retrofitted by 1.4 mm thick CFRP plates were slightly higher than those of their counterpart beams with 1.2 mm thick CFRP plates, except the two beams tested at 80°C.

Table 2 Load capacities of the specimens at the initial and ultimate debonding

Specimens	Initiation of debonding (kN)	Ultimate debonding (kN)
BnP1.2T-20	23.5	61.8
BnP1.4T-20	37.5	69.2
BnP1.2T0	32.9	64.0
BnP1.4T0	43.9	68.0
BnP1.2T30	65.5	75.4
BnP1.4T30	65.0	88.5
BnP1.2T45	79.1	83.0
BnP1.4T45	81.0	85.9
BnP1.2T60	72.7	90.0
BnP1.4T60	85.4	89.9
BnP1.2T80	49.0	71.7
BnP1.4T80	47.0	61.4

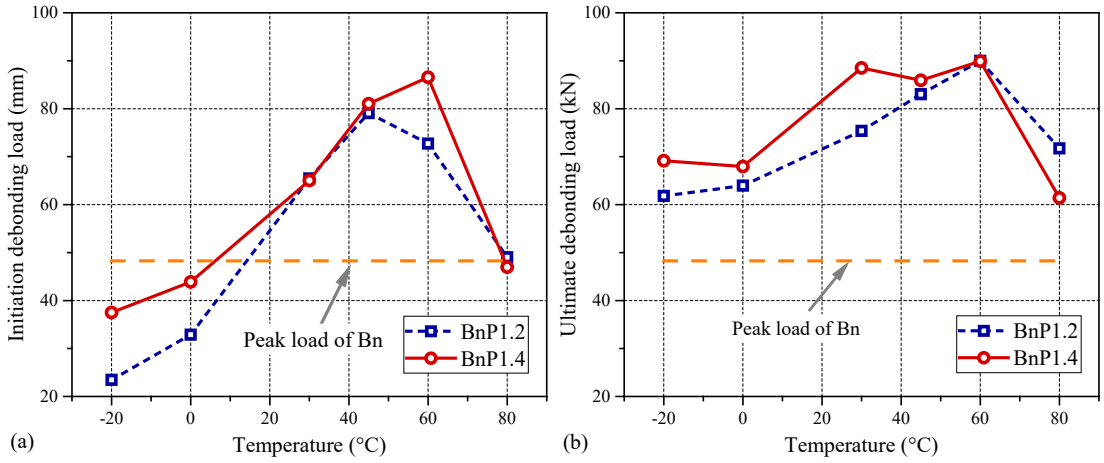

Fig. 14 Comparisons of the load capacities at a) initial debonding and b) ultimate debonding of the CFRP-retrofitted steel beams tested at different service temperatures.

3.3.2. CMOD-load relationships

Fig. 15 compares the changes of CMOD as a function of load at different temperatures. Obviously, the CMOD of the notched steel beam after CFRP retrofitting was significantly

reduced, indicating that the CFRP plate could effectively suppress the opening of the prefabricated notch. However, the effectiveness of CFRP retrofitting was different at various temperatures. Again the best crack-arresting ability was achieved in the temperature range of 30°C to 60°C. **Fig. 16** compares the CMOD values in the specimens tested at different service temperatures given the same load level. At low load levels (e.g., 10 kN and 20 kN), the CMOD values at -20°C and 0°C were smaller than those at normal and high service temperatures (from 30°C to 80°C). At 10 kN and 20 kN, the bondline was still in the elastic stage and the only difference of the bondline was its elastic modulus. Therefore, the smaller CMOD could be attributed to the higher elastic modulus of the bonding adhesive at low temperatures. In comparison, after the applied load exceeded 40 kN, the CMOD at low temperatures (-20°C and 0°C) was much higher than that at the normal temperature (30°C). This was due to the initiation of local interfacial debonding near the notch, which reduced the strengthening efficiency of the CFRP plate in arresting the crack opening at the notch location. In addition, the CMODs at high service temperatures (45°C, 60°C and 80°C) were higher than that at 30°C at all load levels due to the reduction of the elastic modulus of the adhesive with the temperature increase. The local interfacial debonding at 80°C under 60 kN further increased the CMOD.

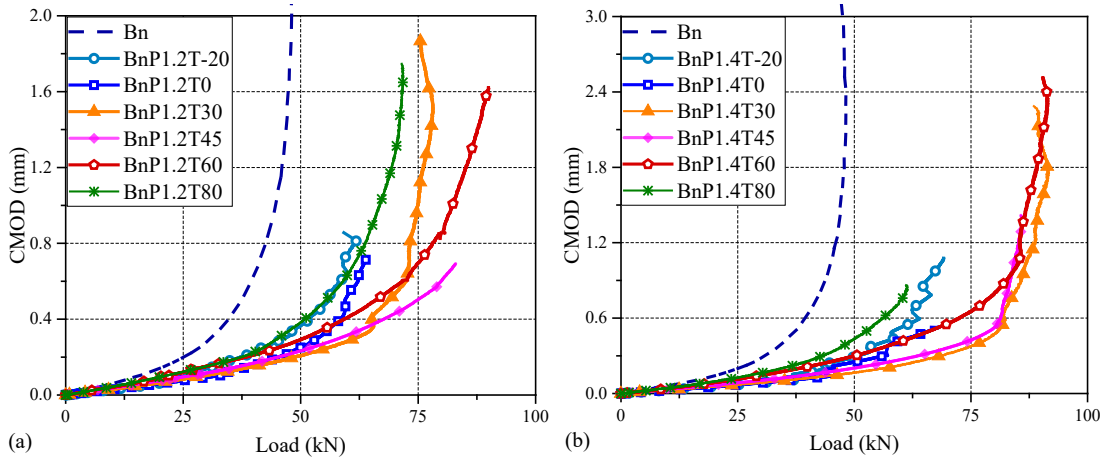

Fig. 15 CMOD-load curves of the specimens tested at different temperatures: a) strengthened with a 1.2 mm CFRP plate; b) strengthened with a 1.4 mm CFRP plate.

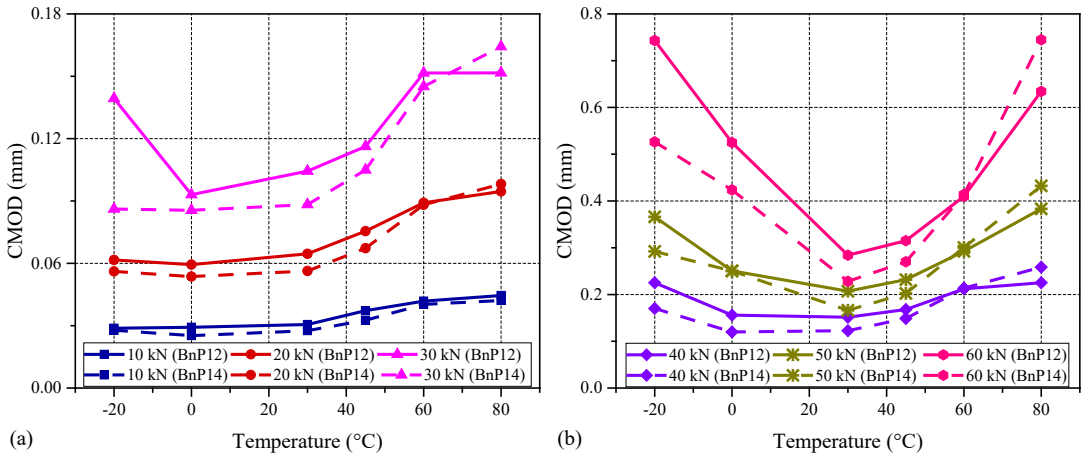

Fig. 16 Comparison of crack-opening displacements at various temperatures and constant mechanical loading: a) 10 kN to 30 kN; b) 40 kN to 60 kN.

3.3.3. Distributions of CFRP strains and interfacial shear stresses

Taking a load level of 20 kN as an example, **Fig. 17** shows the strain distributions in the CFRP plate at different temperatures. It can be seen that the strain values at various temperatures were similar in the notched section but were very different at the locations far from the notched section. Specifically, the magnitudes of CFRP strain at -20°C and 0°C were even negative near the plate ends due to the different thermal shrinkages of the CFRP plate and steel beam. In addition, a dramatic increase in CFRP strains could be seen near the notch. The strain values in the CFRP plate at 80°C were positive near the plate ends and the slope of the strains near the notch was much lower, suggesting that the stress concentration near the notch section was alleviated due to the softening of the bonding adhesive at high temperatures.

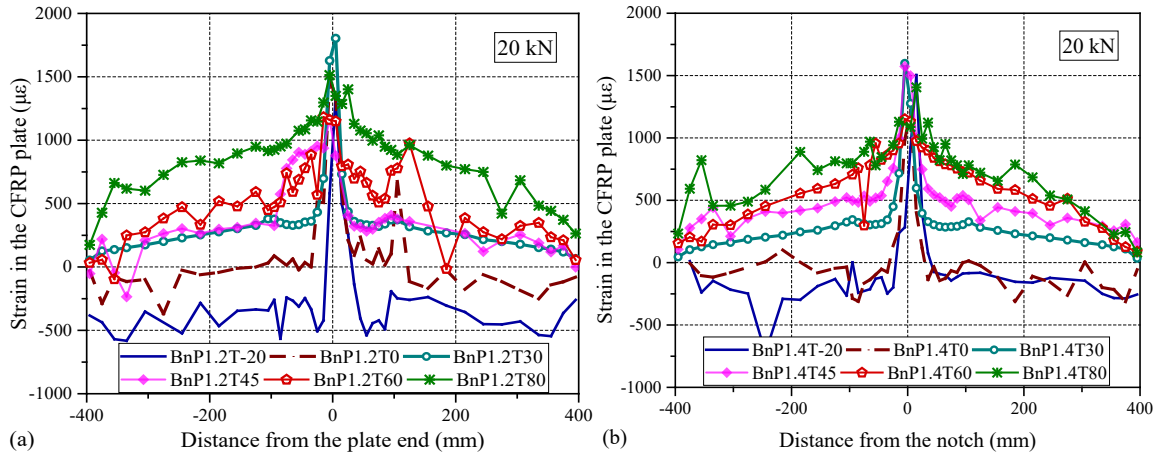

Fig. 17 Distributions of CFRP strains at different temperatures under 20 kN: a) BnP1.2; b) BnP1.4.

Fig. 18 shows the distributions of the interfacial shear stresses under 20 kN at different temperatures. It is seen that in most cases, the interfacial shear stresses were higher near both the notch and plate ends, despite some fluctuations due to the accumulated measurement error

of the CFRP strain during the heating/cooling period. This indicates that the interfaces were still in the *E* stage. In addition, the magnitudes of interfacial shear stresses near the notch at high service temperatures (i.e., 45°C, 60°C, 80°C) were lower than those at low (i.e., -20°C, 0°C) and normal temperatures (i.e., 30°C), because of the thermally-induced softening of the bonding material.

Fig. 19 shows the strain distributions in the CFRP plate under a higher level of mechanical loading (i.e., 60 kN) at different temperatures. It is evident that the strain values in the CFRP plate increased significantly as compared to those at 20 kN (**Fig. 17**). In addition, for the specimens tested in the temperature range of 30°C to 60°C, the strains in the CFRP plate increased almost linearly from the plate end to the notch location where the maximum value was reached, implying that the bondline in these cases was still in its elastic stage. However, the locally debonded zone could be observed for the specimens tested at -20°C, 0°C and 80°C at 60 kN, as indicated by the flat strains in the CFRP plate with large values. Especially for BnP1.2T-20, it is seen that the length of the debonded zone on the right side was comparable to the total length of the CFRP plate, indicating that the ultimate debonding failure was approaching.

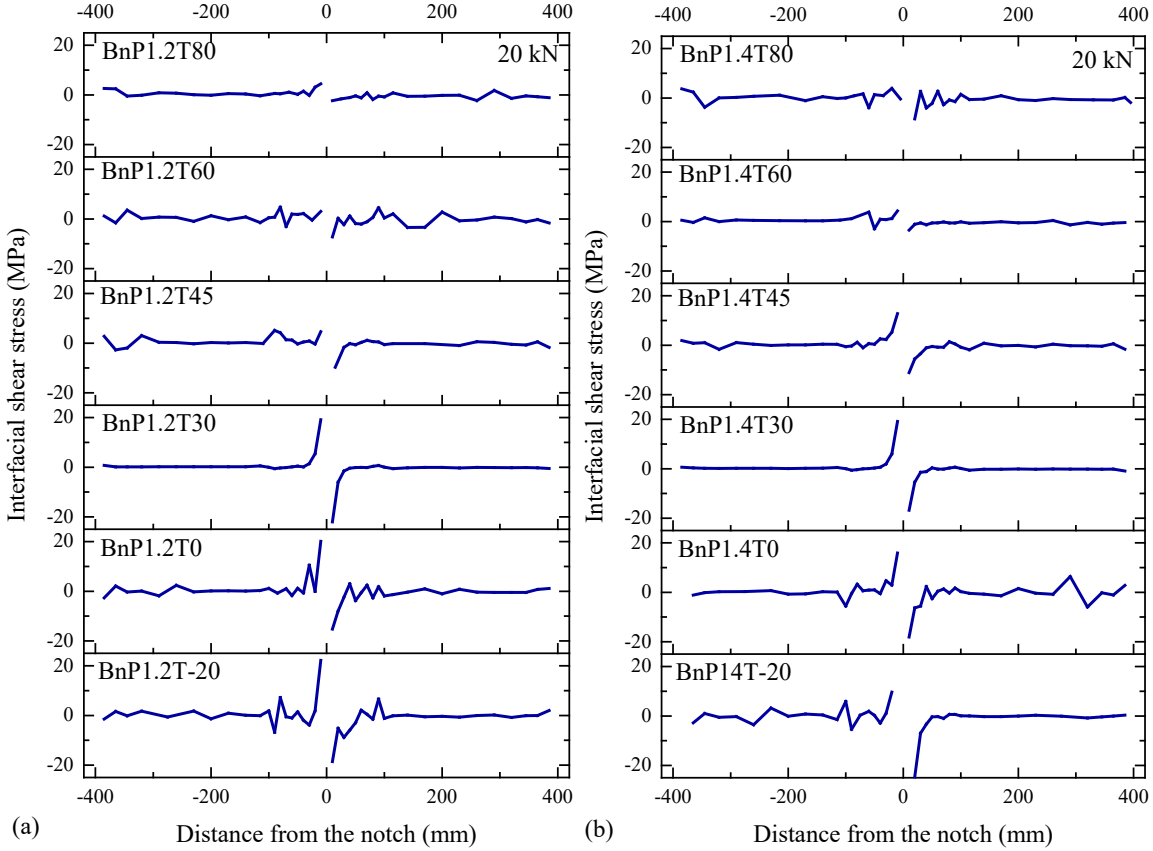

Fig. 18 Distributions of interfacial shear stresses at different temperatures under 20 kN: a) BnP1.2; b) BnP1.4.

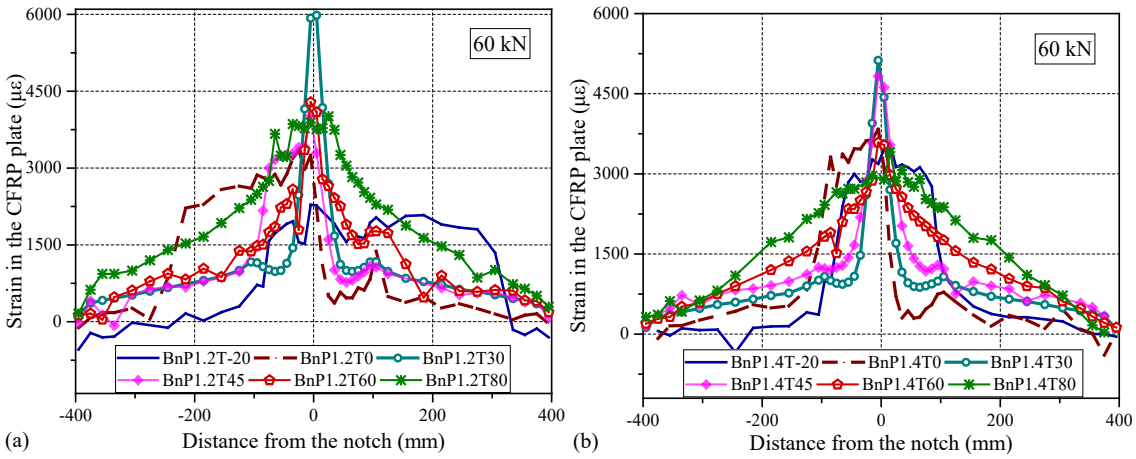

Fig. 19 Distributions of CFRP strains at different temperatures under 60 kN: a) BnP1.2; b) BnP1.4.

Fig. 20 shows the distributions of interfacial shear stresses at different temperatures under 60 kN. In this figure, the solid lines describe the distributions of interfacial shear stresses in the *E* and *E-S* zones, whereas the dash lines show the distribution of interfacial shear stress in the locally debonded zone. It can be observed that the interfacial shear stresses increased rapidly in the area near the notch in the temperature range of 30°C to 60°C, which meant that the bondline interface was still in its elastic deformation stage. However, for the specimens tested at -20°C, 0°C and 80°C, the debonded region was observed at one or both sides of the notch. In the debonded zones, the interfacial shear stresses decreased to almost zero. The softening and elastic zones could be clearly differentiated near the side of the debonded zone.

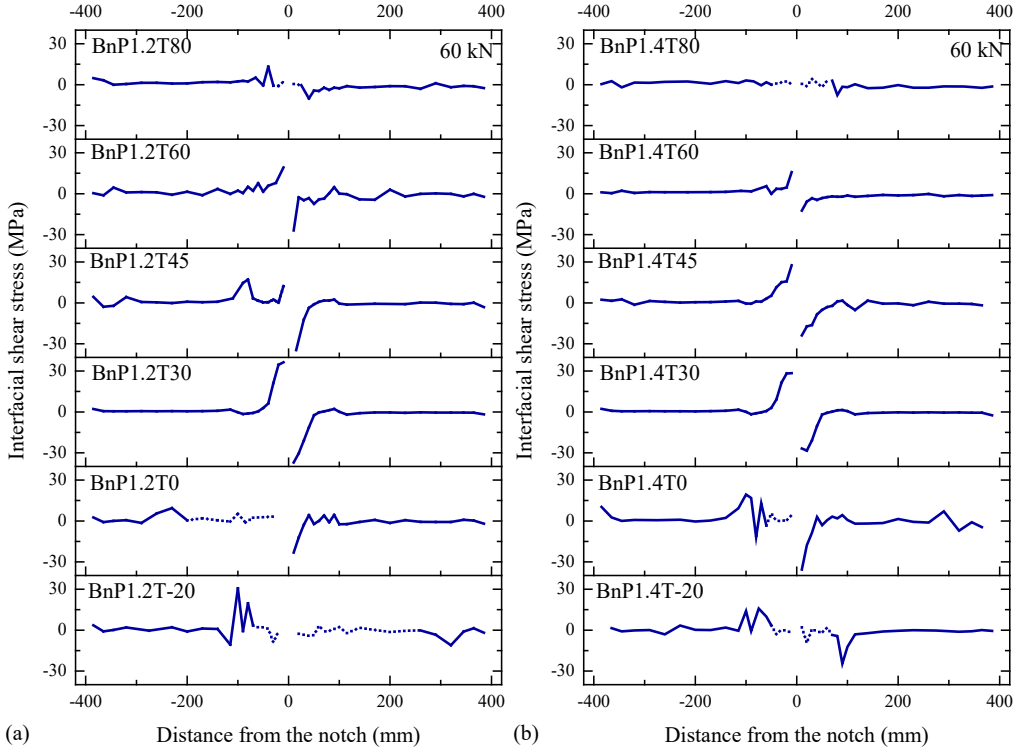

Fig. 20 Distributions of interfacial shear stresses at different temperatures under 20 kN: a) BnP1.2; b) BnP1.4.

Fig. 21 shows the peak values of the interfacial shear stresses experienced by the bondline at various locations near the ultimate state (i.e., close to the ultimate debonding). The dashed lines in this figure illustrate that the regions exhibited distinct softening and debonding stages in terms of the local bond-slip behavior. It can be observed that the peak interfacial shear stresses were generally high and fluctuated a lot near the notch section, probably due to the local compressive stress in the direction normal to the interface near the notch [11]. In comparison, the peak interfacial shear stresses away from the notch section were relatively close, which experienced obvious *E* and *E-S* stages. The hollow symbols in this figure represent the data points with close peak stresses, which are used to derive the representative local bond-slip relationship of the beam specimen. For some specimens (e.g., BnP1.4T80, BnP1.2T60, BnP1.2T45, BnP1.4T0), the interfacial debonding propagated abruptly from the notched section to the plate end. In this case, the CFRP plate strains during the propagation of interfacial debonding could not be monitored, and as a result, the representative local bond-slip behaviors of these specimens are not provided in the following subsection.

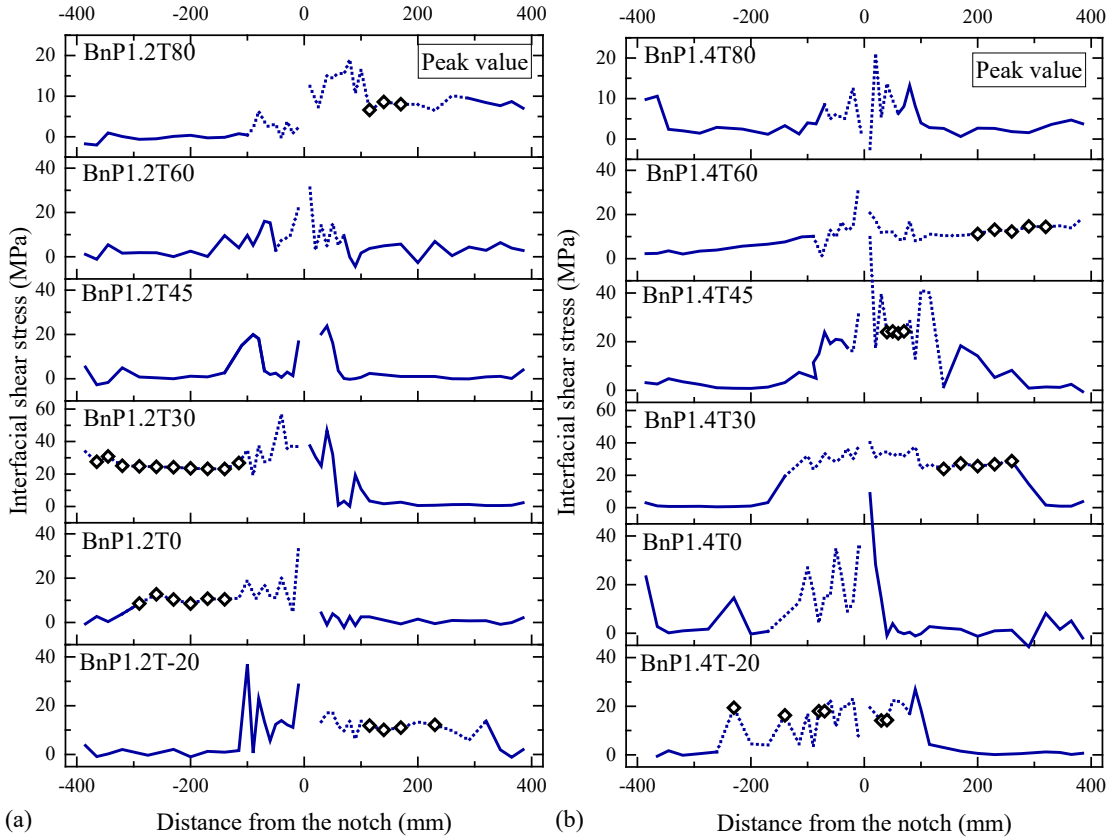

Fig. 21 Distributions of the peak values of interfacial shear stresses at different temperatures: a) BnP1.2; b) BnP1.4.

3.4. Local bond-slip behavior at different temperatures

3.4.1. Determination of the interfacial slips

The above analyses showed that the interfacial bond behaviors of the CFRP-retrofitted steel beams are quite different at various temperatures. When determining the bond-slip relationship, the values of interfacial shear stresses can be derived by Eq. (1) and special attention should be paid to how the interfacial shear slips are determined.

In the previous study [18], the interfacial slips along the bondline were derived according to the formula proposed by Alexander and Cheng [64]. In this method, the difference of the interfacial slips ($\delta_{i+\frac{1}{2}} - \delta_{i-\frac{1}{2}}$) between two points (i.e., $x_{i-\frac{1}{2}}$ and $x_{i+\frac{1}{2}}$) was calculated by integrating the strain in the CFRP plate along the length between these two points. Meanwhile, the CFRP strain (ε_{fi}), which was measured by the strain gauge located at $x = x_i$ and between the two considered points (i.e., $x_{i-\frac{1}{2}}$, $x_{i+\frac{1}{2}}$), was approximately taken as the average strain in this region. Then the slip difference ($\delta_{i+\frac{1}{2}} - \delta_{i-\frac{1}{2}}$) can be calculated by multiplying the measured FRP strain (ε_{fi}) with the distance between the two points (i.e., $x_{i+\frac{1}{2}} - x_{i-\frac{1}{2}}$).

$$\delta_{i+\frac{1}{2}} = \delta_{i-\frac{1}{2}} + \varepsilon_{fi}(x_{i+\frac{1}{2}} - x_{i-\frac{1}{2}}) \tag{2}$$

where ε_{fi} is the measured strain in the CFRP plate at x_i; x_i is the location of the strain gauge. Then the interfacial slip at $x_{i+\frac{1}{2}}$ can be calculated by accumulating the interfacial slips starting from $x_{\frac{1}{2}}$.

$$\delta_{i+\frac{1}{2}} = \delta_{\frac{1}{2}} + \sum_1^i \varepsilon_{fi}(x_{i+\frac{1}{2}} - x_{i-\frac{1}{2}}) \tag{3}$$

Later on, Biscaia *et al.* [65] proposed a new formula for deriving the interfacial slips between FRP and steel/concrete substrate under combined mechanical and thermal loading, in which the thermal deformations of the adherends were considered. As indicated in the previous analytical studies [33,66-68], the interfacial shear slip was defined as the difference of axial deformations between the CFRP plate and the steel/concrete substrate. However, in the above-mentioned two methods [64,65], only the strains in the CFRP plates were considered in deriving the interfacial slip, and the deformation of the concrete/steel substrate was ignored by assuming that the substrate is rigid. Such an assumption may be appropriate for the FRP-to-steel/concrete bonded joints, considering that the steel substrate is under a Mode II shear loading without bending deformation. However, for the CFRP-retrofitted steel beam, the substrate beam is subject to flexural loading and the bending deformation-induced tensile strain at the beam soffit is significant. Therefore, the interfacial slip should be calculated by

integrating the strain difference between the CFRP plate and the beam soffit. Therefore, Eq. (3) should be modified as follows:

$$\delta_{i+\frac{1}{2}} = \delta_{\frac{1}{2}} + \sum_1^i (\varepsilon_{fi} - \varepsilon_{si})(x_{i+\frac{1}{2}} - x_{i-\frac{1}{2}}) \quad (4)$$

where ε_{fi} and ε_{si} is the axial strain of the CFRP plate and steel beam soffit at the location of the strain gauge (x_i). ε_{si} can be calculated considering the deformation of steel beam under bending, axial loading and thermal loading by the following equation [48,49]:

$$\varepsilon_{si} = \frac{y_s}{E_s I_s} M_{si} - \frac{1}{E_s A_s} N_{si} + \alpha_s \Delta T \quad (5)$$

where M_{si} and N_{si} are the bending moment and axial force sustained by the steel beam at $x = x_i$. I_s, A_s and E_s are the second moment of inertia, sectional area and elastic modulus of the steel beam, respectively. y_s is the distance between the neutral axis and the bottom surface of the steel beam. ΔT is the magnitude of temperature variation. Considering the force equilibrium of the CFRP-retrofitted steel beam in its axial direction,

$$N_{fi} = N_{si} \quad (6)$$

where N_{fi} is the axial force resisted by the CFRP plate at ($x = x_i$). N_{fi} can be calculated by the measured axial strain in the CFRP plate (ε_{fi}) based on the following equation:

$$N_{fi} = (\varepsilon_{fi} - \alpha_f \Delta T) E_f A_f \quad (7)$$

The moment equilibrium of the CFRP-retrofitted steel beam at $x = x_i$ can be expressed as follows:

$$M_{Ti} = M_{si} + N_{fi}(y_s + y_f + t_a) \quad (8)$$

where M_{Ti} is the total moment resisted by the retrofitted steel beam at x_i. y_f is the distance from the neutral axis of the CFRP plate to the outer surface of the adhesive layer. t_a is the thickness of the adhesive layer.

By substituting Eqs. (6)-(8) into Eq. (5), the strain at the steel beam soffit can be obtained as:

$$\varepsilon_{si} = \frac{y_s}{E_s I_s} M_{Ti} - \frac{y_s}{E_s I_s}\left(y_s + y_f + t_a\right) N_{fi} - \varepsilon_{fi}(x) + \left(\alpha_f + \alpha_s\right)\Delta T \quad (9)$$

For simplicity:

$$\varepsilon_{si} = \beta_1 M_{Ti} - \beta_2 \varepsilon_{fi} + \beta_3 \Delta T \quad (10)$$

where $\beta_1 = \frac{y_1}{E_1 I_1}$; $\beta_2 = \frac{y_s E_f A_f}{E_s I_s}\left(y_s + y_f + t_a\right) + \frac{E_f A_f}{E_s A_s}$; and $\beta_3 = \beta_2 \alpha_f + \alpha_s$. The detailed derivation process of the above formulae can be found in Refs. [48,49]. Note that in the above equation, β_1, β_2 and ΔT are constants for the specimen tested at a specific service temperature, while M_{Ti} can be calculated by the applied loads.

Finally, by substituting Eq. (10) into Eq. (4), $\delta_{i+\frac{1}{2}}$ can be computed by the following equation:

$$\delta_{i+\frac{1}{2}} = \delta_{\frac{1}{2}} + \sum_1^i [\varepsilon_{fi}(1+\beta_2) - \beta_1 M_{Ti} - \beta_3 \Delta T](x_{i+\frac{1}{2}} - x_{i-\frac{1}{2}}) \quad (11)$$

To validate the reliability and accuracy of the above formula, **Fig. 22** compares the resultant distributions of the interfacial slips along the bond length calculated from the previous formula [64], the newly proposed formula (i.e., Eq. 11) and the FE modeling [48]. For calculating the interfacial slips, the parameters adopted in the studied case and the measured strains in the CFRP plate were all taken from the previous FE modeling [48]. It seems that the previous formula [64] leads to an overestimation of the interfacial slips and the formula proposed in this paper gives the results much closer to the FE predictions.

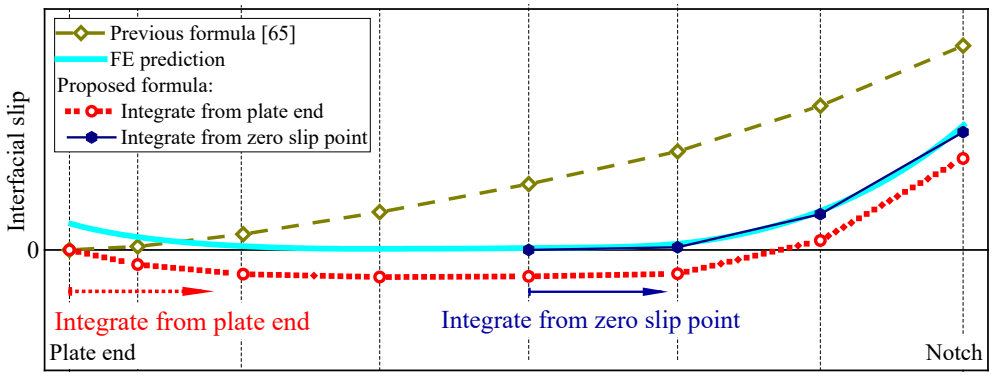

Fig. 22 Comparison of the interfacial slips obtained from different methods.

Note that when the proposed formula is used for deriving the interfacial slip distribution, another consideration is the selection of the first integration point. As shown in **Fig. 22**, if the interfacial slip is integrated from the plate end by setting the interfacial slip at the plate end as zero, the calculated values of interfacial slips would be negative in the region near the plate end, where the strain of the steel beam bottom is higher than that of the CFRP plate (i.e., $\varepsilon_{fi} - \varepsilon_{si}$ is negative). In reality, the interfacial slip at the plate end is not zero (see the FE prediction in **Fig. 22**), and the values of interfacial slips decrease to almost zero as the distance from the plate end increases. Therefore, it is more appropriate to set the first integrating point at the position where the value is equal to zero or a sufficiently small positive value (mainly because the position of the strain gauge cannot exactly correspond to the zero point), so that the slips obtained by the strain integration can be consistent with the FE prediction (see **Fig. 22**).

As clearly seen in **Fig. 22**, the resultant interfacial slips increase gradually from the first integration point to the notch and obtain the maximum value at the notch. The sum of interfacial slips derived from two sides of the notch (i.e., at x = -2.5 mm and x = 2.5 mm) is the CMOD of the notch. Therefore, the CMOD at the notched section measured by the extensometer can

be used to further validate the proposed formula for calculating the interfacial slips. **Fig. 23** compares the sum of interfacial slips derived from the two sides of the notch based on the previous formula [64] and the formulae proposed in this paper as well as the CMOD values measured by the extensometers for BnP1.2T30, BnP1.2T80, BnP1.4T-20 and BnP1.4T60. Note that due to the imposition of different temperatures, the CMOD values measured by the extensometers needed to be initialized to zero to eliminate possible thermally induced values. For ease of comparison, the interfacial slips derived based on the proposed formula were also initialized to zero at 0 kN. It is seen that the proposed formula gives much better predictions, indicating that the assumption of a rigid substrate (i.e., ignoring the bending deformation of the steel beam by the previous formula [64]) is inaccurate for deriving the interfacial slips of the CFRP-retrofitted steel beam.

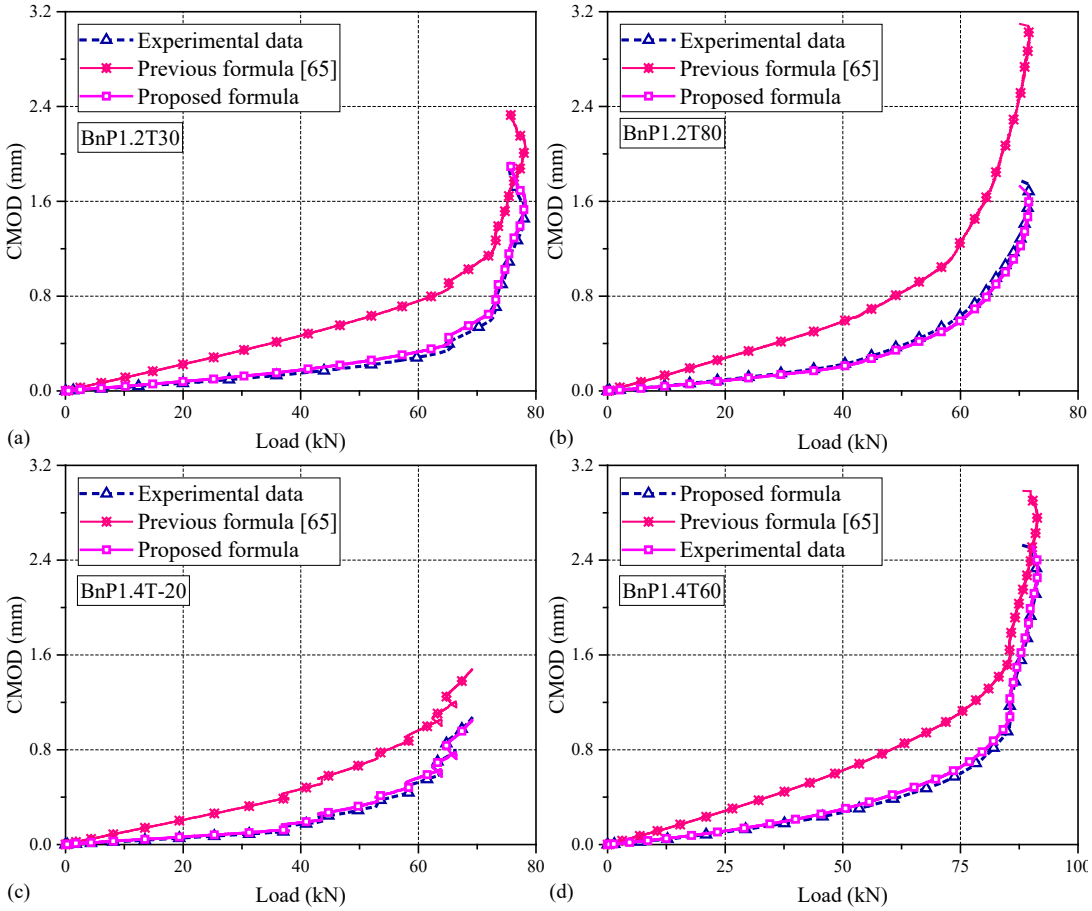

Fig. 23 Comparison of the CMOD values measured by the extensometers and those derived by different formulae: a) BnP1.2T30; b) BnP1.2T80; c) BnP1.4T-20; d) BnP1.4T60.

3.4.2. Comparison of local bond-slip relationships at different temperatures

Fig. 24 compares the derived local bond-slip relationships along the bond length obtained from BnP1.2T30. The interfacial stresses and slips were calculated using Eqs. (1) and (11), respectively. It can be observed that the bond-slip relationships at different locations are quite

different. Specifically, the bond interface near the notch (i.e., from -30 mm to 30 mm) generally exhibited an elastic-plastic-softening behavior, which varied dramatically within this region. This could be attributed to the effect of the interfacial compressive stress [2] that enhanced the local bond in the mode-II direction. In the previous research on analyzing the bond behavior between the CFRP plate and concrete/steel substrate under a mixed-mode loading [38,40,50,68], the effect of tensile stress in the mode-I direction was usually considered because it decreased the mode-II bond strength. A similar phenomenon was also reported in the previous experimental study on the bond behavior of FRCM composites using direct shear and modified beam tests [69]. It was found that the interfacial compressive stresses produced in the modified beam tests tended to enhance the utilization efficiency of the FRP strength and to reduce the interfacial slips, as compared to those observed in the direct shear tests. However, there was still a lack of study on the effect of interfacial compressive stress on the mode-II bond behavior.

Fig. 24b shows that the bond interface exhibited almost the consistent bond behavior at locations farther from the notch and stiffeners (i.e., from -365 mm to -115 mm), where the normal interfacial stresses were marginal [2]. This phenomenon was widely observed in the specimens conducted at normal and elevated temperatures. In this paper, only the locations with similar local bond behaviors and far away from the notch section were considered for determining the representative local bond-slip relationships. These locations are indicated using the symbols in **Fig. 21**.

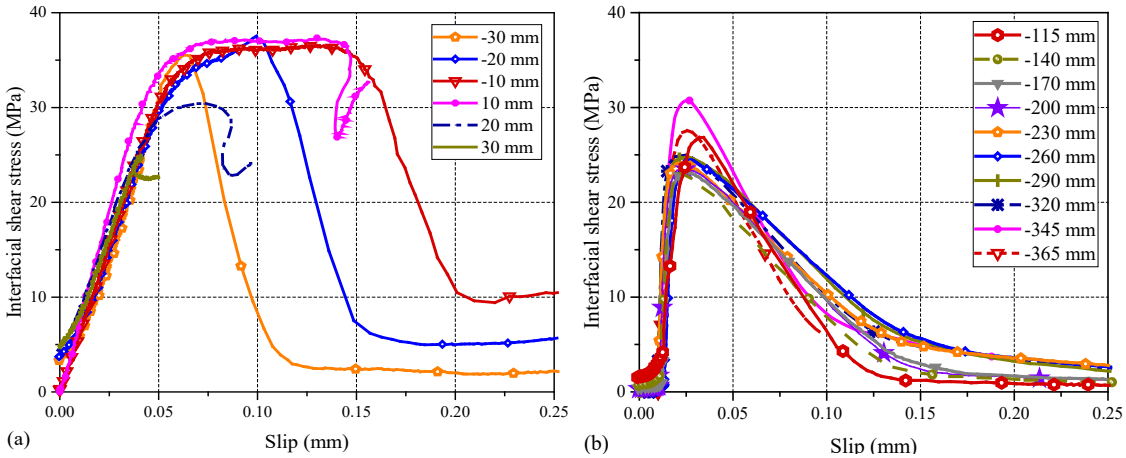

Fig. 24 The local bond-slip relationships obtained at different locations in BnP1.2T30: a) from -30 mm to 30 mm; b) from -365 mm to -115 mm.

Fig. 25Fig. shows the derived representative bond-slip relationships of BnP1.2T30. The dashed lines are the bond-slip curves derived based on the nonlinear regression analysis using MATLAB curve fitting box (smoothing splines with the smoothing parameter set as 0.9999),

which was also used by Zhou *et al.*'s [18] to derive the bond-slip curves. It is clear that the regressed bond-slip relationships show obvious ascending (elastic stage) and descending (softening stage) branches. Therefore, a bilinear bond-slip model with linear elastic and softening stages was used herein to describe the local bond behavior in the CFRP-retrofitted steel beams. The interfacial shear stiffnesses (i.e., slopes) in both elastic and softening stages were calculated based on the linear fitting method, and the interfacial fracture energy (G_f) was calculated as the area underneath the regressed bond-slip curves. Then, the peak shear stress could be calculated from the determined fracture energy and the stiffnesses of the elastic and softening branches. The resulting bilinear bond-slip relationships are shown by the solid black line in **Fig. 25**.

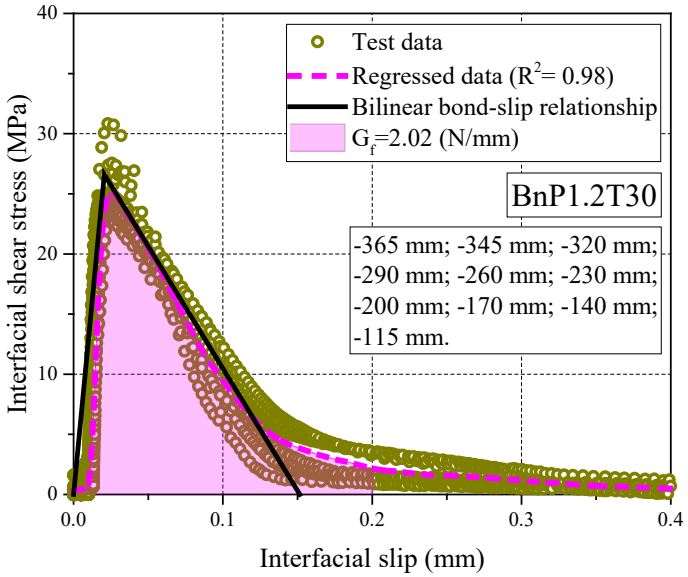

Fig. 25 The representative local bond-slip relationships of BnP1.2T30.

The derived representative bond-slip relationships of some other specimens are shown in the **Fig. A1** of the Appendix to ensure that the paper is written more concisely. The derived parameters of the bilinear bond-slip relationships at different temperatures are summarized in **Table 3**. The bond properties of the CFRP-to-steel interface changed significantly with the temperature variations, in terms of elastic stiffness (i.e., interfacial shear stiffness of the elastic branch), peak shear stress and interfacial fracture energy. **Fig. 26** compares the elastic stiffness with the storage modulus of the bonding material at various temperatures. It is seen that the interfacial shear stiffness decreases as the temperature increases, generally following the variation of the elastic modulus of the bonding adhesive, indicating the thermally-induced deterioration of the material from a solid glassy to a viscous softening state.

Table 3 The parameters of the bilinear bond-slip relationship at different temperatures

Specimens	Elastic stiffness (MPa/mm)	Peak shear stress (MPa)	Interfacial fracture energy (N/mm)
BnP1.2T-20	998.6	10.64	0.34
BnP1.4T-20	1078.8	18.86	0.53
BnP1.2T0	905.0	12.34	0.44
BnP1.2T30	1292.3	26.61	2.02
BnP1.4T30	1266.7	28.99	2.50
BnP1.4T45	308.0	22.68	2.91
BnP1.4T60	66.5	13.69	3.20
BnP1.2T80	26.0	7.02	1.22

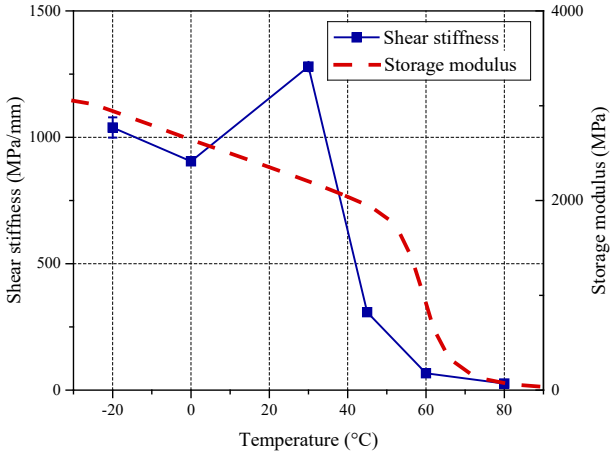

Fig. 26 Interfacial elastic stiffness and measured storage modulus of the bonding material at different temperatures.

Fig. 27 shows the changes of peak shear stress and interfacial fracture energy as the temperature increases. The peak shear stress and interfacial fracture energy were much lower at both low and high service temperatures. Moreover, the interfacial fracture energy increased from 30°C to 60°C, while the peak shear stress decreased during this temperature range. The change of the debonding load of CFRP-retrofitted steel beams (**Fig. 14**) was quite close to the change of the interfacial fracture energy as the temperature varied (**Fig. 27b**) rather than the change of peak shear stress (**Fig. 27a**).

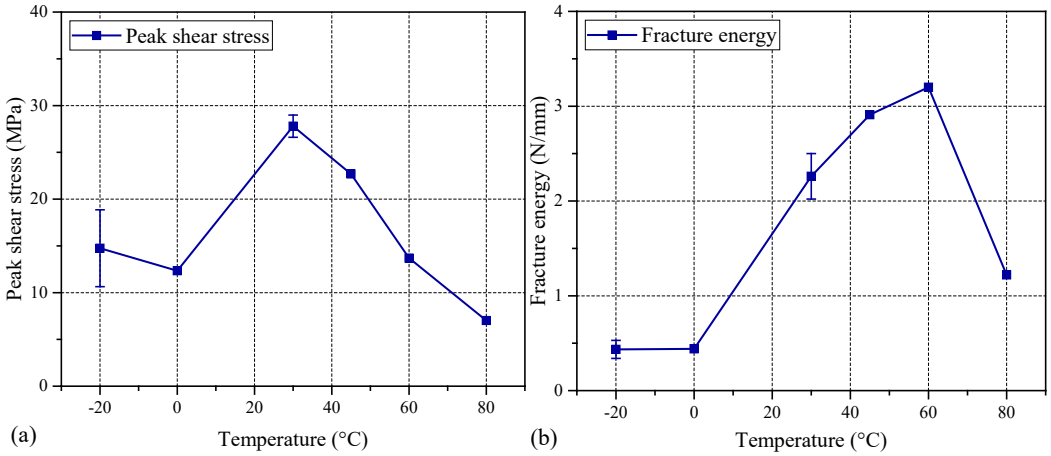

Fig. 27 Changes of the bond properties at different temperatures: (a) peak shear stress; (b) interfacial fracture energy.

4. Finite Element (FE) Model

4.1. Description of the FE model

For better interpreting the structural performance and the IC debonding mechanism of CFRP-retrofitted steel beams at different temperatures, two-dimensional finite element (FE) modeling was conducted using the commercial software ABAQUS 6.14 based on the plane stress assumption. The schematic of FE modeling is shown in **Fig. 28**. The CFRP plate and the steel beam were modeled by 4-node plane stress quadrilateral (CPS4R) elements. The different widths at different heights of the specimen (i.e., web, flange, adhesive layer and CFRP plate) were considered by adopting different out-of-plane thicknesses. The adhesive layer was modeled by 4-node two-dimensional cohesive (COH2D4) elements. The element sizes of the adherends and the adhesive layer were set as 0.2 mm in the *x*-direction [47]. The ABAQUS software has been successfully used by the authors' group for modeling the FRP-strengthened steel/concrete beams at both normal and high temperatures (exposed to fire) [38,70-73], and therefore, the element types and size as well as the definitions of material properties and boundary conditions are all determined based on the previous experience. The reference temperature (i.e., 30°C) was set in the initial step. The target service temperature was defined by the predefined field variable in the second step, which was uniformly distributed in the specimen. The beams were loaded in a displacement-controlled manner as the third step.

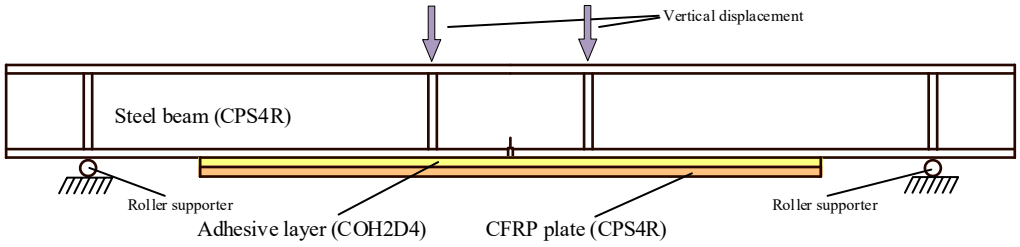

Fig. 28 Schematic of the FE model.

The material properties of the steel obtained from the tensile coupon tests are the engineering (nominal) stress and strain values. These engineering stresses (σ_e) are calculated by dividing the measured tensile forces (F) by the original cross-sectional area (A_0), while the engineering strains (ε_e) are determined by dividing the measured deformations (δ) by the initial gauge length (L_0). The engineering stress-strain values cannot be used directly as input data in the numerical analysis because they are only valid before necking. Therefore, the ABAQUS software adopts true (Cauchy) stresses and logarithmic strains for FE modeling of the steel material. The true stress (σ_t) and logarithmic strain (ε_t) can be computed by the following functions [74,75]:

$$\sigma_t = \sigma_e \times (1 + \varepsilon_e) \quad (12)$$

$$\varepsilon_t = ln(1 + \varepsilon_e) \quad (13)$$

where σ_e is the nominal stress and ε_e is the nominal strain; both are obtained from the tensile coupon tests. **Fig. 28** compares the nominal stress-strain curves of the steel obtained from three tensile coupon tests with the stress-strain relationship used in the FE model. The yielding strength in the nominal stress-strain relationship is determined as 359 MPa and inputted into the FE model. After the steel has yielded, the strain hardening modulus (E') is set as 2700 N/mm^2 according to the suggestion provided in Ref. [76], which was also used in the previous FE model of CFRP-retrofitted steel beams and was shown to achieve excellent FE predictions of the load-deflection responses [28,40]. In the current FE model, the von-Mises yield surface criterion specified in ABAQUS is used to define the initiation of plastic flow of the steel material under a biaxial stress state. The J_2 flow rule is then used to determine the stress increment due to the strain growths during the plastic deformation.

The possible crack propagation of the steel along the prefabricated notch in the steel beam web is modeled by the extending finite element method (XFEM), which was widely used in the FE modelings of metallic structures, such as steel pressure vessels and piping [77], steel pipelines [78-82] and aluminum plates [83]. The onset of damage of the steel material after the in-plane principal stress reaches its maximum value (σ_{maxps}) (**Fig. 28**). Then a damage variable evolves linearly with the plastic strain, and the crack propagates until the energy dissipated per unit area reaches the specified fracture energy (G_f) during the damage evolution process. In the previous studies, the recommended values of σ_{maxps} and G_f were found to be affected by the material properties of steel and the specimen geometry [84], and thus they were usually estimated by a trial-and-error calibration method using experimental results [80-82].

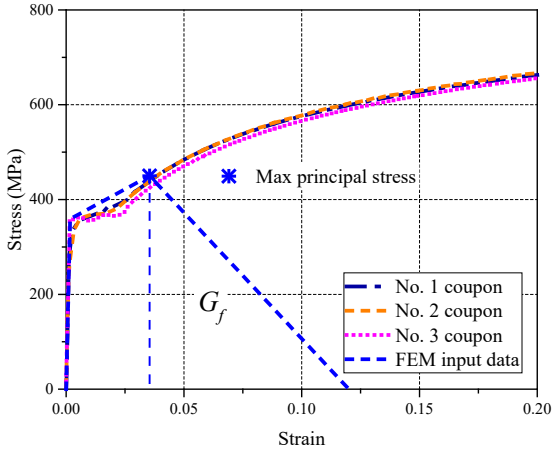

Fig. 28 The nominal and input stress-strain relationships of the steel.

According to the experimental observations, at large CMODs, the necking phenomenon is observed around the notch tip (i.e., as the out-of-plane thickness of the steel decreases) due

to the intensified stress concentration. Therefore, using the engineering stress-strain relationship and ignoring the necking effect in the FE model will significantly underestimate the deflections and CMODs of the notched steel beam under bending loading. In the literature, in order to more closely simulate the structural performance of the notched steel beam without retrofitting, accurate values of σ_{maxps} and G_f were obtained by trial-and-error analysis to best predict the load-deflection and CMOD-load curves [80-82]. In the current FE model, a similar approach is used, and the exact values of σ_{maxps} and G_f are determined to be 450 MPa and 3.3×10^3 N/mm, respectively. **Table 4** summarizes the material parameters of steel adopted in the FE model.

Table 4 Material parameters of steel

Elastic modulus (E) (GPa)	Yielding stress (f_y) (MPa)	Maximum principal stress (σ_{maxps}) (MPa)	Strain hardening modulus (E') (MPa)	Fracture energy (G_f) (N/mm)	Coefficient of thermal expansion (α_s) (/°C)
210.5	359	450	2700	3300	1.14×10^{-5}

The load-deflection and CMOD-load curves predicted by the FE model are compared with the experimental results in **Fig. 29**. It is clearly seen that using the material parameters of steel defined in **Table 1**, the structural performance of the un-strengthened notched steel beam can be accurately predicted by the proposed FE model.

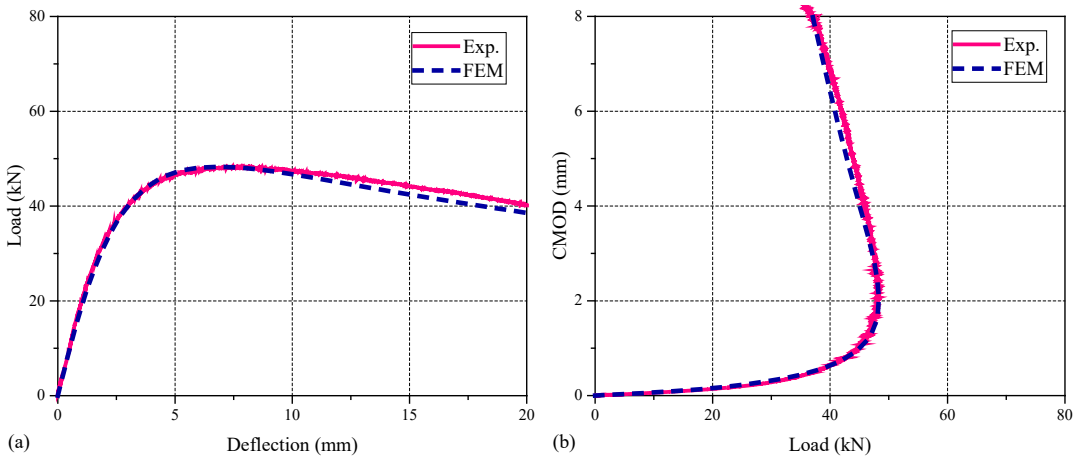

Fig. 29 Comparison of the structural performance of the notched steel beam obtained from the experimental test and the FE model: a) load-deflection curves; b) CMOD-load curves.

The CFRP plate is defined as an orthotropic material. The elastic modulus in the axial direction (E_1) is obtained from the coupon tests. Other parameters, including the elastic moduli in the other two directions (E_2, E_3), Poisson's ratios (v_{12}, v_{13}, v_{23}) and shear modulus (G_{12},

G_{13}, G_{23}) are taken from the previous study [38], in which a similar CFRP plate was used. The material parameters of the CFRP plate adopted in the FE model are shown in **Table 5**.

Table 5 Material parameters of CFRP plate

CFRP plate	Elastic modulus (E_1) (GPa)	Elastic modulus (E_2&E_3) (GPa)	Poisson's ratio (v_{12}, v_{13})	Poisson's ratio (v_{23})	Shear modulus (G_{12}&G_{22}) (GPa)	Shear modulus (G_{23}) (GPa)	Coefficient of thermal expansion (α_f) (/°C)
1.2T	171.32	10	0.3	0.0058	25.5	3.6	-9.10×10^{-7}
1.4T	158.18	10	0.3	0.0058	25.5	3.6	-8.48×10^{-7}

The bond parameters determined at various temperatures shown in **Table 3** are used to define the bilinear bond-slip behavior of the CFRP-to-steel interface in the mode II direction. The bond behavior in the mode I direction is also simplified as a bilinear bond-separation relationship, whose parameters are determined from the tensile tests of the adhesive coupons. According to the test data, the tensile strength and elastic modulus of the adhesive at normal temperature are 49.7 MPa and 2.55 GPa, respectively. Therefore, the peak interfacial normal stress and interfacial tensile stiffness are determined as 49.7 MPa and 6.89 GPa/mm. Furthermore, the slope of the softening branch of the bond-separation relationship is set to be 12.8 times that of the elastic branch (i.e., interfacial normal stiffness in **Table 6**), as suggested by the previous FE modeling [40]. In addition, the changes of the parameters (e.g., the interfacial normal stiffness and the interfacial fracture energy) of the bond-separation behavior in the mode-I direction at different temperatures are determined to be the same as the corresponding parameters in the mode-II direction as described in **Table 3**. The resulting values used to define the bond behavior in the mode-I direction at different temperatures are summarized in **Table 6**.

Table 6 The interfacial bond parameters in the mode-I direction

Specimens	Interfacial normal stiffness (MPa/mm)	Peak normal stress (MPa)	Interfacial fracture energy (N/mm)
BnP1.2T-20	5378.6	17.13	0.0295
BnP1.4T-20	5810.8	22.14	0.0456
BnP1.2T0	4874.7	18.43	0.0376
BnP1.2T30	6891.9	49.70	0.194
BnP1.4T30	6891.9	49.70	0.194
BnP1.4T45	1659.2	27.68	0.249
BnP1.4T60	358.1	13.49	0.274
BnP1.2T80	140.1	5.20	0.105

4.2 Validation of the FE model

4.2.1 Comparisons of the load-displacement responses

Fig. 30 compares the experimental and FE predicted load-displacement curves of four representative CFRP-retrofitted steel beams at different temperatures. More comparisons are provided in **Fig. A2** of the Appendix. The data points at the onset of debonding and the ultimate debonding are marked in the figure. The initial debonding load in the FE analysis is determined when the interfacial shear stress at the notch location is reduced to zero. The ultimate debonding load in the FE modeling is ascertained when the predicted length of the debonded region is identical to that measured during the experiment in the ultimate debonding state. It is seen that the load-deflection curves predicted by the FE model are in good agreement with the experimental results, which has verified the reliability of the FE model and the adopted local bond-slip relationships of the CFRP-to-steel interface at different temperatures. It is noteworthy that at -20°C and 0°C, the flexural stiffness of CFRP-strengthened steel beams predicted by the FE model after the onset of interfacial debonding is lower than the experimental data (**Fig. 30a & Fig. A2 a, b, c**). This difference is mainly due to the ignorance of possible enhancement in the steel properties at low service temperatures. As reported in the previous study [85], the elastic modulus and yield strength of the conventional steel material were increased by 1.8% and 9.4% respectively, when the service temperature was reduced from 20°C to -10°C. These enhancements were further increased to 4.9% and 18.1% as the temperature decreased to -30°C. Overall, the FE model can give reasonably good predictions of the load-displacement curves of the CFRP-retrofitted notched steel beams tested at different service temperatures.

Fig. 31 further compares the load capacities from the experimental tests and the FE predictions at initiation and ultimate debonding states. It is observed that the changing trends of the load capacities at different temperatures can be well captured by the FE model.

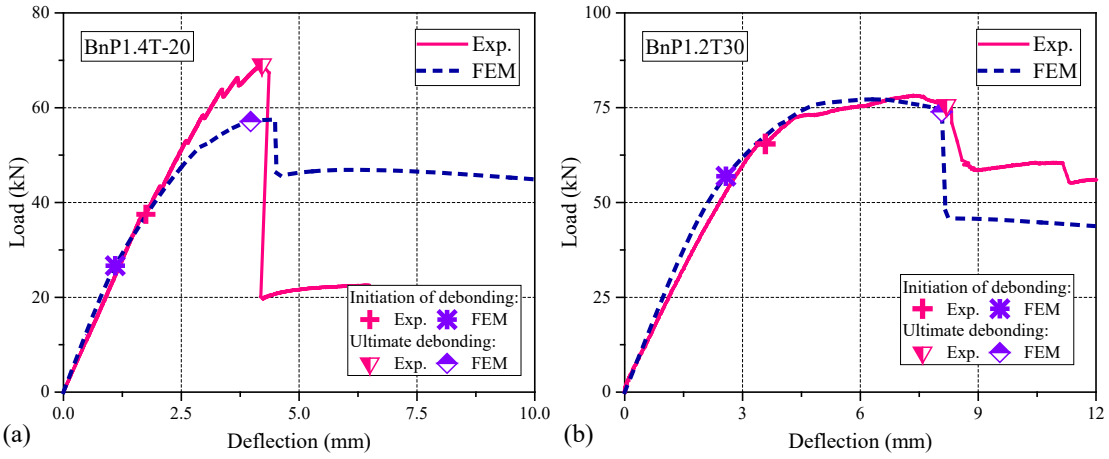

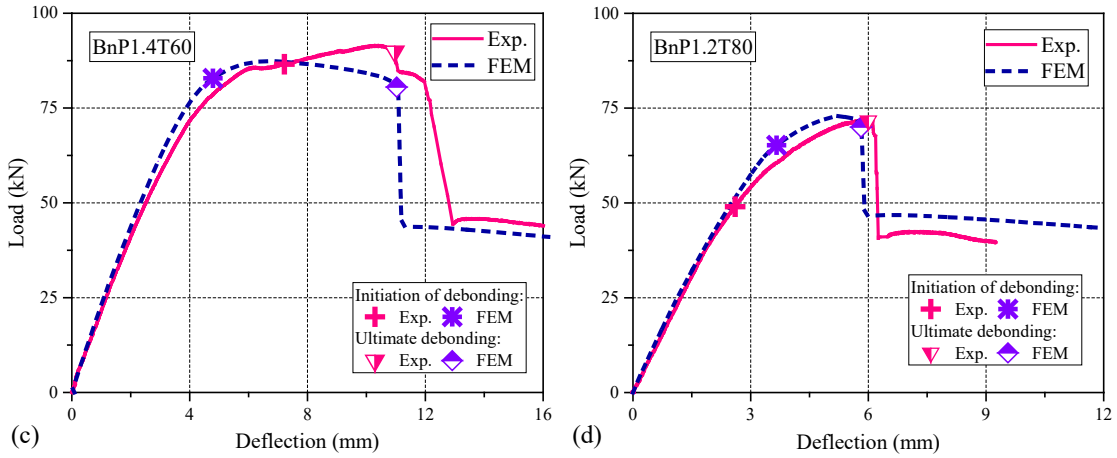

Fig. 30 Comparisons of load-deflection curves obtained from experiments and FE modeling: a) BnP1.4T-20; b) BnP1.2T30; c) BnP1.4T60; d) BnP1.2T80.

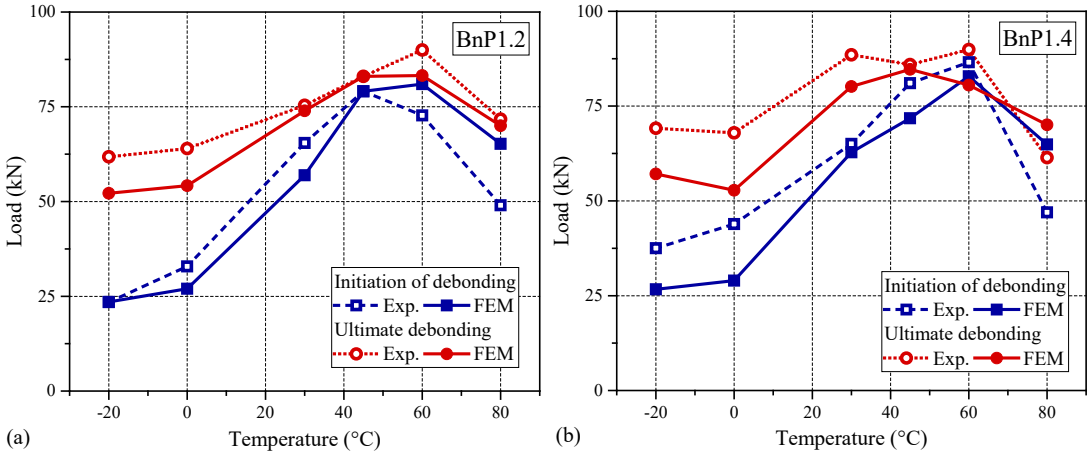

Fig. 31 Comparisons of load capacities at initiation and ultimate debonding states obtained from experiments and FE modeling: a) BnP1.2; b) BnP1.4.

4.2.2. Comparisons of the CMOD-load curves

Fig. 32 shows the comparisons between the experimental and FE predicted CMOD-load curves of CFRP-retrofitted steel beams at different temperatures. The FE results also agree well with the experimental data, indicating that the crack-opening behavior in the strengthened beams can be accurately predicted.

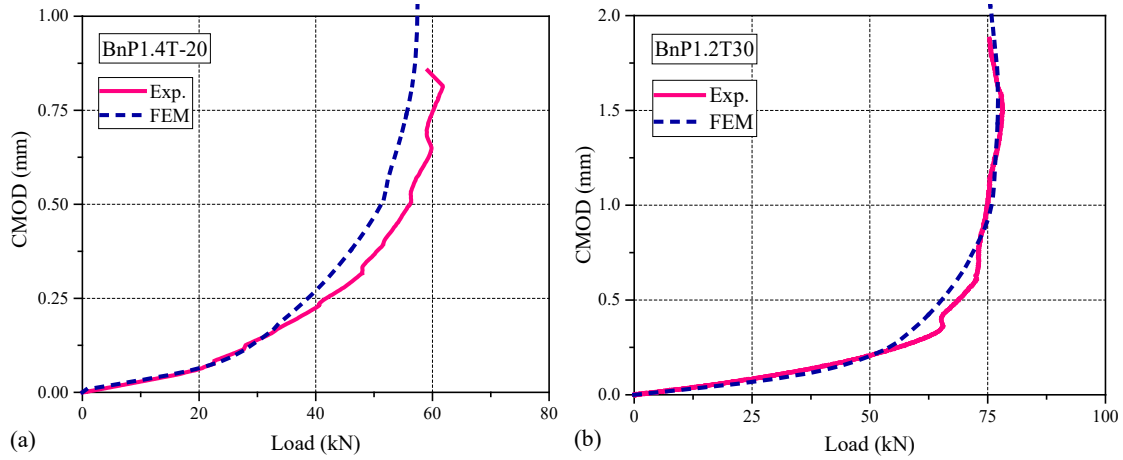

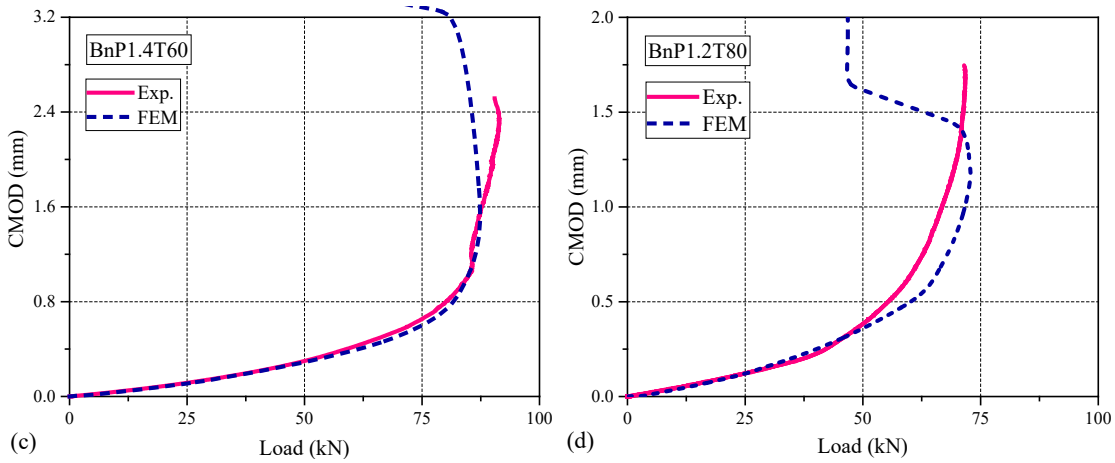

Fig. 32 Comparison of CMOD-load relationships obtained from experiments and FE modeling: a) BnP1.4T-20; b) BnP1.2T30; c) BnP1.4T60; d) BnP1.2T80.

4.2.3. Comparisons of the strain distributions in the CFRP plate

Fig. 33 shows the experimental and FE predicted strain distributions in the CFRP plate before applying the mechanical loading at two extreme temperatures (i.e., -20 and 80°C). It is important to note that the thermal deformation of the specimen is small, and the accuracy of the strain gauges is sensitive to these small values. Therefore, the measured CFRP strains exhibit significant fluctuations. Nevertheless, overall, the predicted CFRP strains are in close agreement with the measured data.

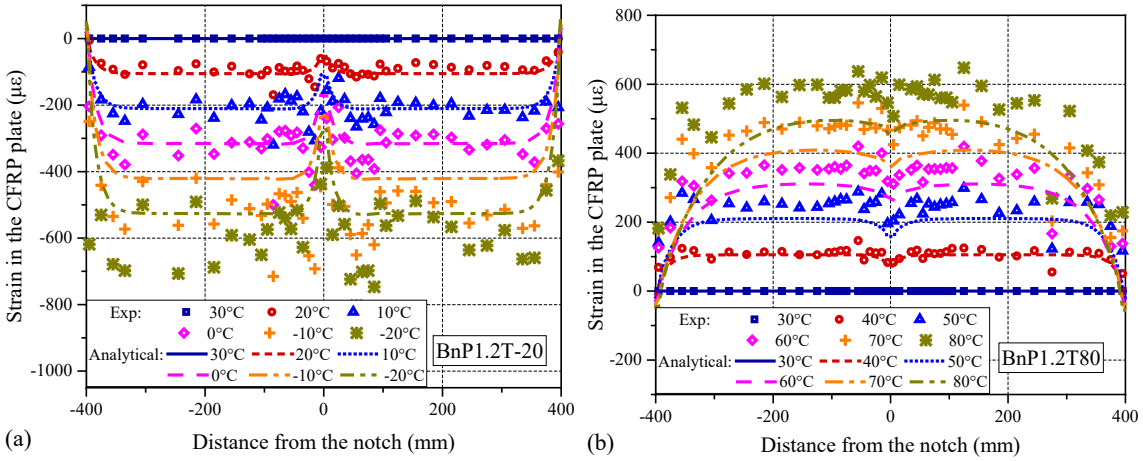

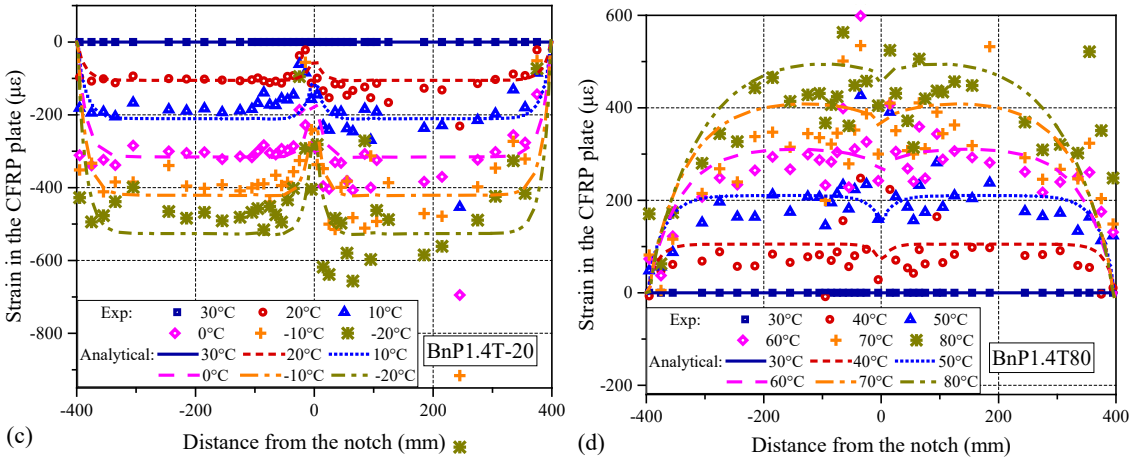

Fig. 33 Comparison of the experimental and FE predicted strain distributions in the CFRP plate under thermal loading only: a) BnP1.2T-20; b) BnP1.2T80; c) BnP1.4T-20; d) BnP1.4T80.

Fig. 34 compares the strain distributions in the CFRP plate at various load levels obtained from the experiments and the FE model predictions in the representative specimens. More test data is provided in **Fig. A3** of the **Appendix**. In general, the agreement is acceptable although relatively large scatters are observed near the notched section, where the enhanced local bond behavior exists as explained earlier. The evolution of deformation stages of the CFRP-retrofitted steel beams, including the *E*, *E-S* and *E-S-D* stages, are all well captured by the FE model.

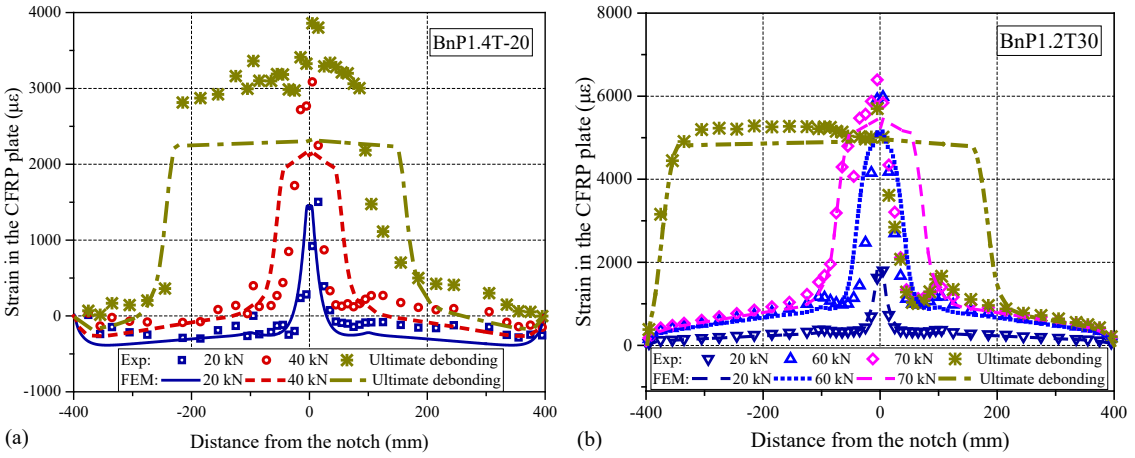

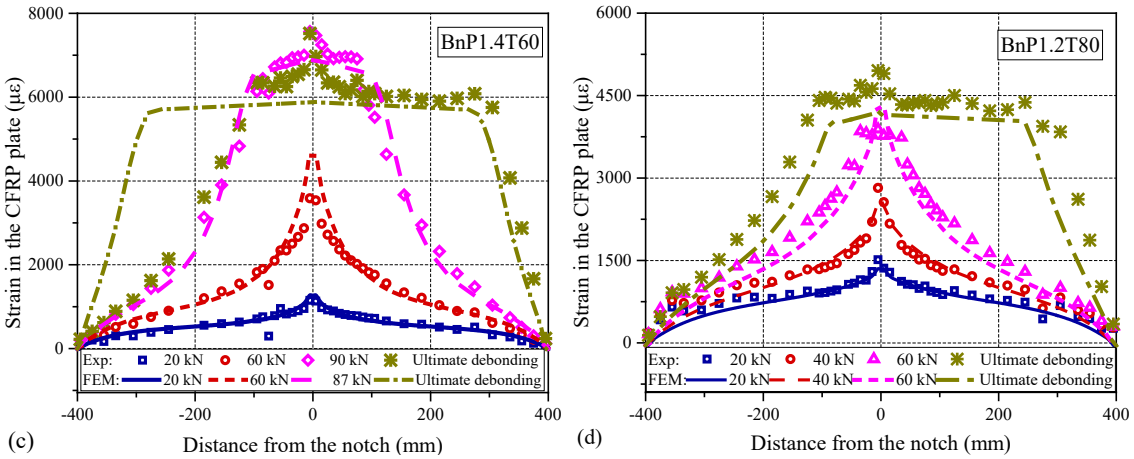

Fig. 34 Comparisons of the experimental and FE predicted strain distributions in the CFRP plate: a) BnP1.4T-20; b) BnP1.2T30; c) BnP1.4T60; d) BnP1.2T80.

5. Conclusions

In this paper, the structural performance of CFRP-retrofitted notched steel beams under flexural loading and the corresponding interfacial behaviors were investigated in the temperature range of -20°C to 80°C. Based on the experimental studies and FE modeling, the following conclusions can be drawn:

(a) When the temperature is changed from -20°C to the glass transition temperature of the bonding adhesive (i.e., 60°C), the average load capacities at the initial and ultimate debonding of the CFRP-retrofitted steel beams are increased by 161% and 37.4%, respectively. However, at a high temperature of 80°C, they decrease by 39.7% and 26.0%, respectively.

(b) The ultimate debonding load of the CFRP-retrofitted steel beam is found to be significantly affected by the interfacial fracture energy of the CFRP-to-steel interface in the mode-II direction.

(c) The strengthening efficiency of the CFRP plate in restricting the CMODs is seriously compromised at both very low (e.g., -20°C, 0°C) and very high (e.g., 80°C) temperatures, because of the increased brittleness of the bonding adhesive at very low temperatures and the reduced interfacial shear stiffness at very high temperatures.

(d) For the local bond-slip behavior of the CFRP-to-steel interface obtained from the experimental study, the changes of interfacial shear stiffness at different temperatures are related to the variations of the elastic modulus of the bonding adhesive. The average interfacial fracture energy increases by 6.3 times from -20°C to 60°C, but decreases by 61.7% at 80°C.

(e) The structural performance of the FRP-retrofitted steel beams at different temperatures can be accurately predicted by the proposed FE model, in which the effects of interfacial thermal stresses and the temperature-dependent bond properties are appropriately considered.

Acknowledgments

The authors would like to acknowledge the financial support supplied by the Nature Science Foundation of China (51978398 and 51478406), the Research Grants Council of the Hong Kong SAR (15219919) and the Natural Science Foundation of Shanghai (19ZR1426200).

Appendix:

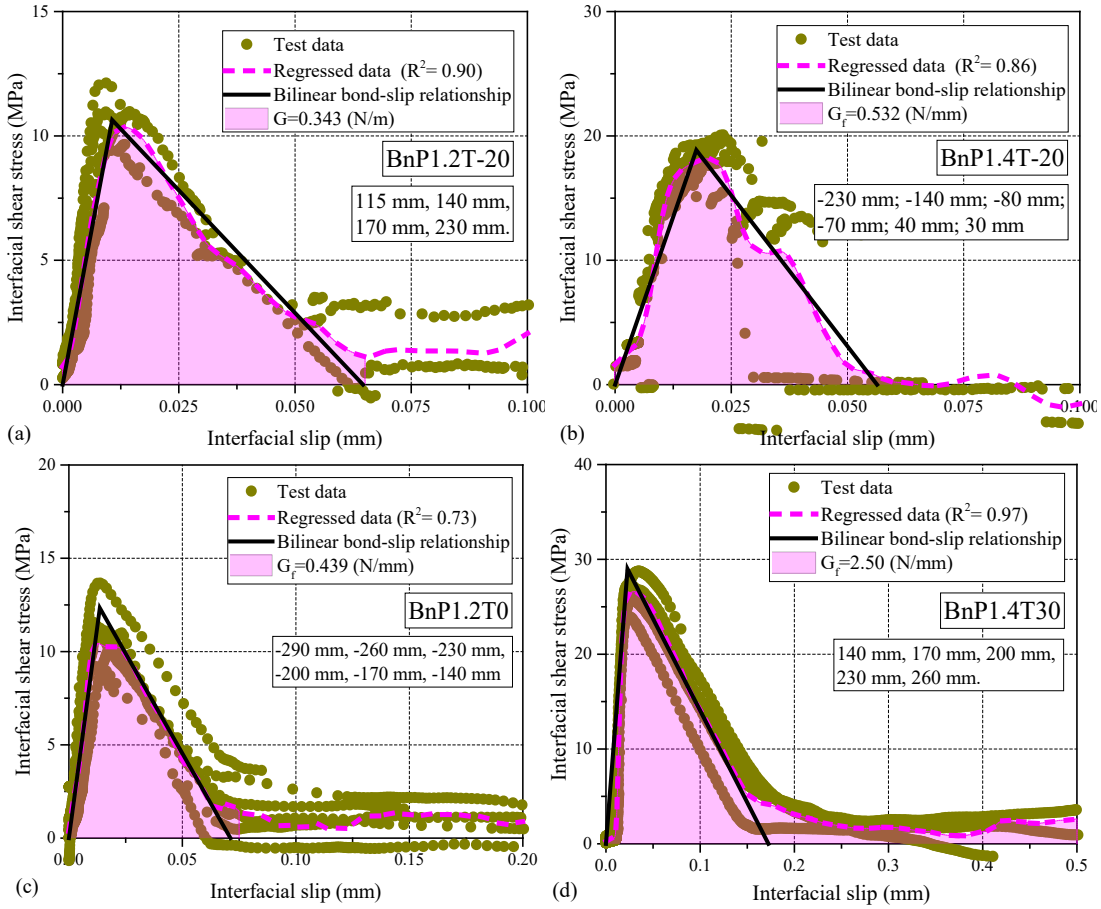

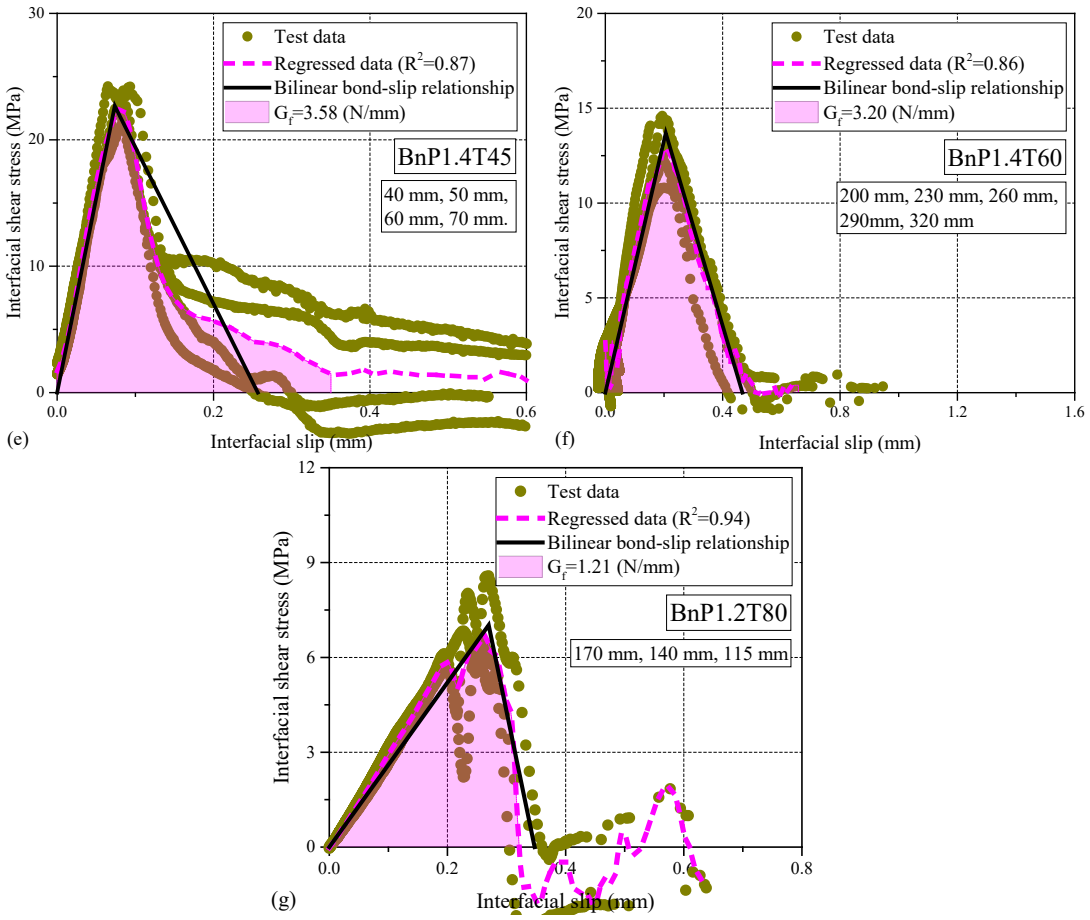

Fig. A1 Local bond-slip relationships of the interface derived from the bending tests of the specimens: a) BnP1.2T-20; b) BnP1.4T-20; c) BnP1.2T0; d) BnP1.4T30; e) BnP1.4T45; f) BnP1.4T60; g) BnP1.2T80.

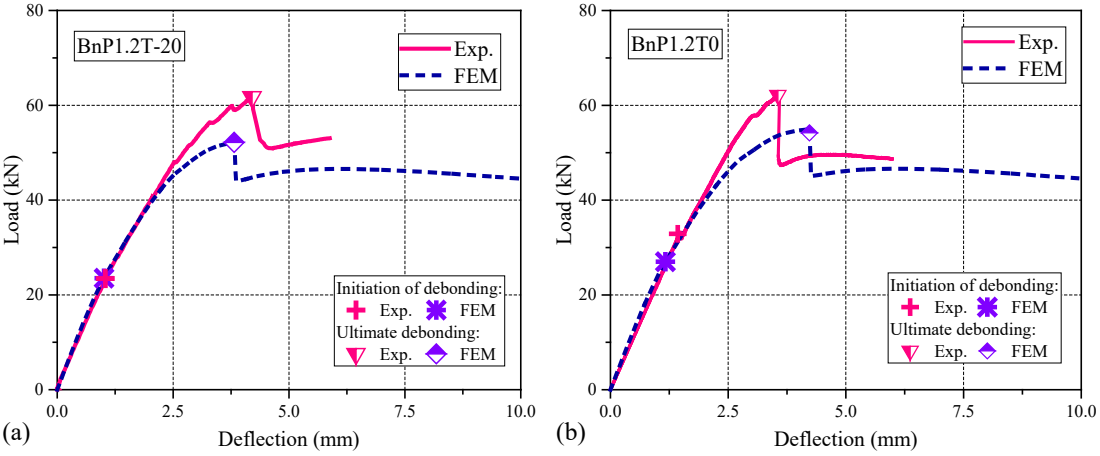

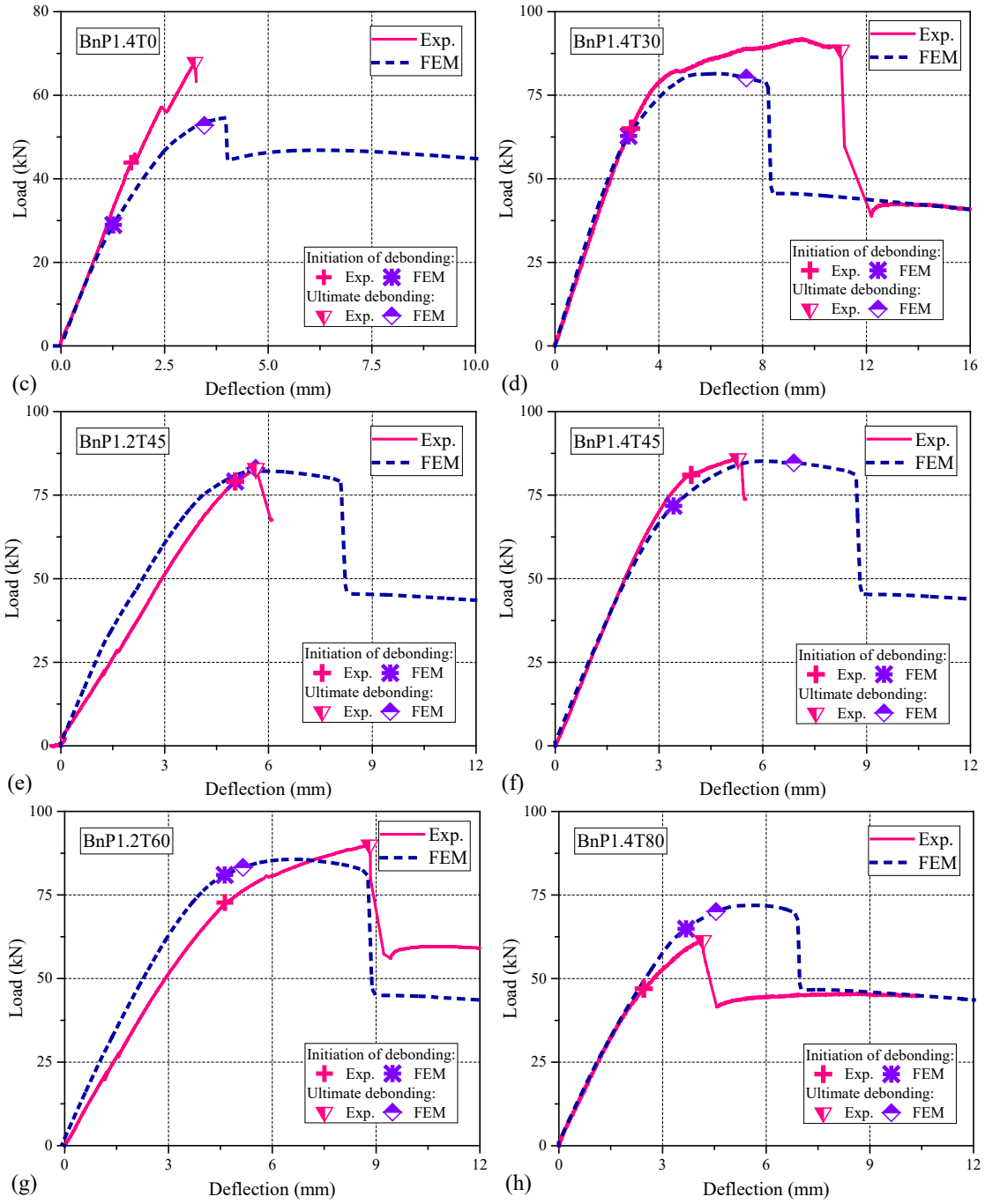

Fig. A2 Comparisons of load-deflection curves between the test data and the FE predictions: a) BnP1.2T-20; b) BnP1.2T0; c) BnP1.4T0; d) BnP1.4T30; e) BnP1.2T45; f) BnP1.4T45; g) BnP1.2T60; h) BnP1.4T80.

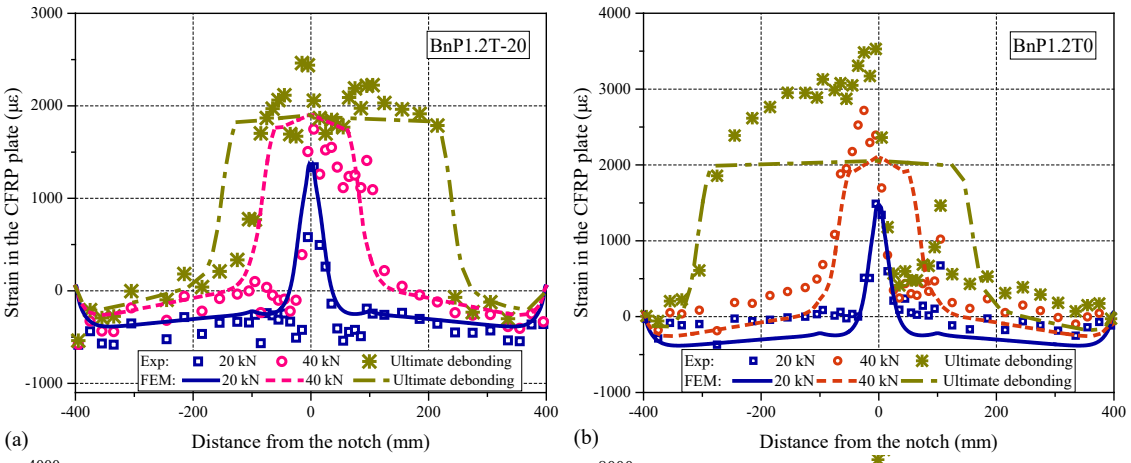

866

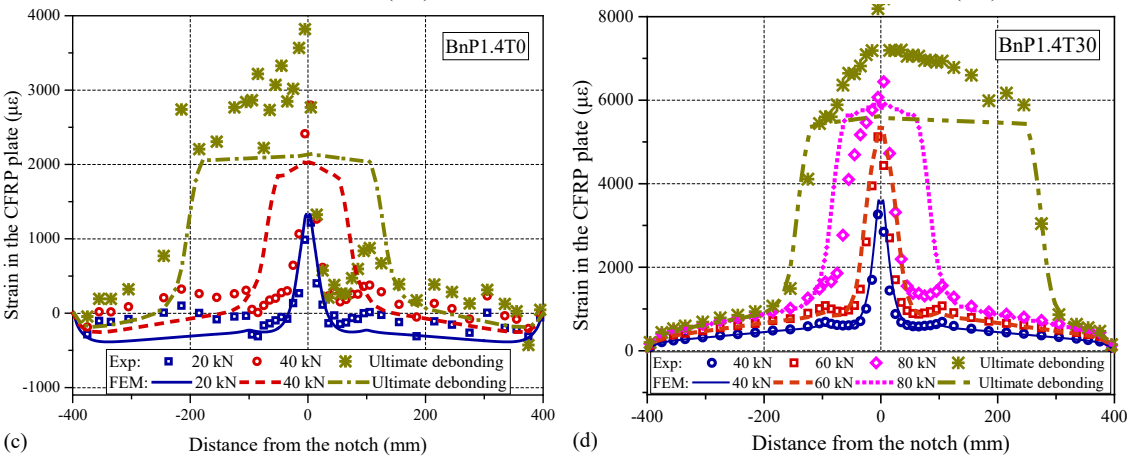

867

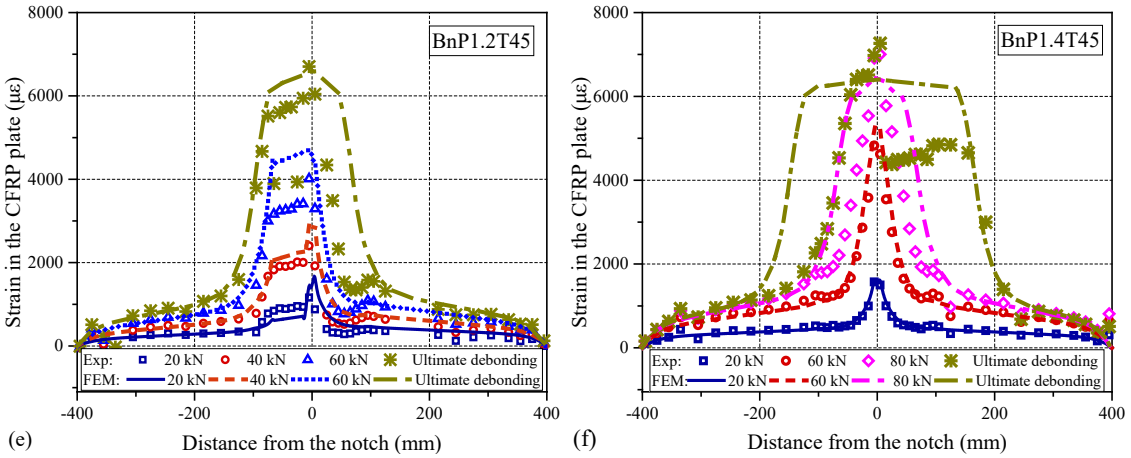

868

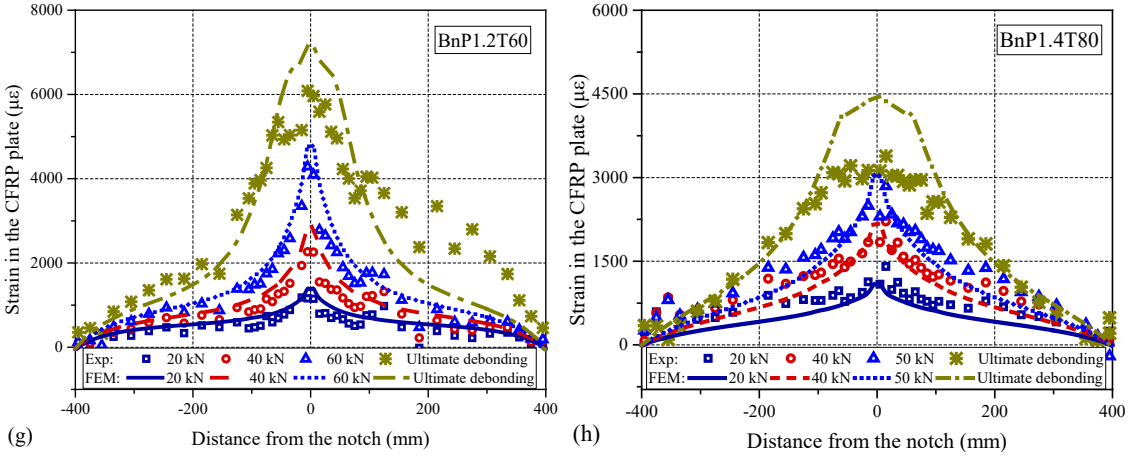

869

Fig. A3 Comparisons of CFRP strain distributions between the test data and the FE predictions: a) BnP1.2T-20; b) BnP1.2T0; c) BnP1.4T0; d) BnP1.4T30; e) BnP1.2T45; f) BnP1.4T45; g) BnP1.2T60; h) BnP1.4T80.

References

[1] Hmidan A, Kim YJ, Yazdani S. CFRP repair of steel beams with various initial crack configurations. J Compos Constr 2011;15(6):952–62.

[2] Deng J, Jia YH, Zheng HZ. Theoretical and experimental study on notched steel beams strengthened with CFRP plate. Compos Struct 2016;136:450–59.

[3] Teng JG, Yu T, Fernando D. Strengthening of steel structures with fiber-reinforced polymer composites. J Constr Steel Res 2012; 78: 131–43.

[4] Wang Y, Zhou C, Li X, Lu Z, Gong F. Experimental study on steel plates with and without notches strengthened by CFRP sheets. J Adhes Sci Technol 2019; 33(17): 1895–1912.

[5] Chen T, Huang C. Fatigue tests on edge cracked four-point bend steel specimens repaired by CFRP. Compos Struct 2019;219:31–41.

[6] Yu QQ, Wu YF. Fatigue strengthening of cracked steel beams with different configurations and materials. J Compos Constr 2017;21(2):04016093.

[7] Yu QQ, Wu YF. Fatigue retrofitting of cracked steel beams with CFRP laminates. Compos Struct 2018;192:232–44.

[8] Colombi P, Fava G. Experimental study on the fatigue behaviour of cracked steel beams repaired with CFRP plates. Eng Fract Mech 2015;145:128–42.

[9] Deng J, Li J, Zhu M. Fatigue behavior of notched steel beams strengthened by a prestressed CFRP plate subjected to wetting/drying cycles. Compos B Eng 2022;230:109491.

[10] Wang Y, Li J, Deng J, Li S. Bond behaviour of CFRP/steel strap joints exposed to overloading fatigue and wetting/drying cycles. Eng Struct 2018;172:1–12.

[11] Deng J, Li JH, Wang Y, Xie WZ. Numerical study on notched steel beams strengthened by CFRP plates. Const Build Mater 2018;163:622–33.

[12] Wang Z, Li C, Sui L, Xian G. Effects of adhesive property and thickness on the bond performance between carbon fiber reinforced polymer laminate and steel. Thin-Walled Struct 2021;158:107176.

[13] Yang Y, Biscaia H, Chastre C, Silva M. Bond characteristics of CFRP-to-steel joints. J Constr Steel Res 2017;138:401–19.

[14] Al-Shawaf A, Zhao XL. Adhesive rheology impact on wet lay-up CFRP/steel joints' behaviour under infrastructural subzero exposures. Compos B Eng 2013;47:207–19.

[15] Biscaia HC, Ribeiro P. A temperature-dependent bond-slip model for CFRP-to-steel joints. Compos Struct 2019;217:186–205.

[16] Al-Shawaf AK. Characterization of bonding behavior between wet lay-up carbon fibre reinforced polymer and steel plates in double-strap joints under extreme environmental temperatures. Australia: Monash University, 2010.

[17] Sahin MU, Dawood M. Experimental investigation of bond between high-modulus CFRP and steel at moderately elevated temperatures. J Compos Constr 2016;20(6):04016049.

[18] Zhou H, Fernando D, Torero JL, Torres JP, Maluk C, Emberley R. Bond behavior of CFRP-to-steel bonded joints at mild temperatures: experimental study. J Compos Constr 2020;24(6):04020070.

[19] Al-Shawaf A, Al-Mahaidi R, Zhao X-L. Effect of elevated temperature on bond behaviour of high modulus CFRP/steel double-strap joints. Aust J Struct Eng 2009;10:63–74.

[20] Chandrathilaka E, Gamage J, Fawzia S. Mechanical characterization of CFRP/steel bond cured and tested at elevated temperature. Compos Struct 2019;207:471–77.

[21] Ke L, Li C, He J, Dong S, Chen C, Jiao Y. Effects of elevated temperatures on mechanical behavior of epoxy adhesives and CFRP-steel hybrid joints. Compos Struct 2020;235:111789.

[22] Korayem AH, Chen SJ, Zhang QH, Li CY, Zhao XL, Duan WH. Failure of CFRP-to-steel double strap joint bonded using carbon nanotubes modified epoxy adhesive at moderately elevated temperatures. Compos B Eng 2016;94:95–101.

[23] Nguyen TC, Bai Y, Zhao XL, Al-Mahaidi R. Mechanical characterization of steel/CFRP double strap joints at elevated temperatures. Compos Struct 2011;93:1604–12.

[24] Bocciarelli M, Colombi P, Fava G, Sonzogni L. Energy-based analytical formulation for the prediction of end debonding in strengthened steel beams. Compos Struct 2016;153:212–21.

[25] Bocciarelli M, Colombi P, D'Antino T, Fava G. Intermediate crack induced debonding in steel beams reinforced with CFRP plates under fatigue loading. Eng Struct 2018;171:883–93.

[26] Liu M, Dawood M. A closed-form solution of the interfacial stresses and strains in steel beams strengthened with externally bonded plates using ductile adhesives. Eng Struct 2018;154:66–77.

[27] Stratford TJ, Bisby LA. Effect of warm temperatures on externally bonded FRP strengthening. J Compos Constr 2012;16:235–44.

[28] Fernando ND. Bond behaviour and debonding failures in CFRP-strengthened steel members: The Hong Kong Polytechnic University, 2010.

[29] He J, Xian G. Debonding of CFRP-to-steel joints with CFRP delamination. Compos Struct 2016;153:12–20.

[30] Yu T, Fernando D, Teng JG, Zhao XL. Experimental study on CFRP-to-steel bonded interfaces. Compos B Eng 2012;43:2279–89.

[31] Dehghani E, Daneshjoo F, Aghakouchak AA, Khaji N. A new bond-slip model for adhesive in CFRP–steel composite systems. Eng Struct 2012;34:447–54.

[32] Fernando D, Yu T, Teng JG. Behavior of CFRP laminates bonded to a steel substrate using a ductile adhesive. J Compos Constr 2014;18(2):04013040.

[33] Deng J, Lee MMK, Moy SSJ. Stress analysis of steel beams reinforced with a bonded CFRP plate. Compos Struct 2004;65:205–15.

[34] Biscaia HC, Borba IS, Silva C, Chastre C. A nonlinear analytical model to predict the full-range debonding process of FRP-to-parent material interfaces free of any mechanical anchorage devices. Compos Struct 2016;138:52–63.

[35] Zhou H, Gao WY, Biscaia HC, Wei XJ, Dai JG. Debonding analysis of FRP-to-concrete interfaces between two adjacent cracks in plated beams under temperature variations. Eng Fract Mech 2022;263:108307.

[36] Zhou H, Torres JP, Fernando D, Law A, Emberley R. The bond behaviour of CFRP-to-steel bonded joints with varying bond properties at elevated temperatures. Eng Struct 2019;183:1121–33.

[37] Dong K, Hu K. Development of bond strength model for CFRP-to-concrete joints at high temperatures. Compos B Eng 2016;95:264–71.

[38] Zeng JJ, Gao WY, Liu F. Interfacial behavior and debonding failures of full-scale CFRP-strengthened H-section steel beams. Compos Struct 2018;201:540–52.

[39] Wang Y, Li J, Deng J, Xie W, Zheng Y. Numerical study on notched steel plate with center hole strengthened by CFRP. J Adhes Sci Technol 2017;32:1066–80.

[40] Teng JG, Fernando D, Yu T. Finite element modelling of debonding failures in steel beams flexurally strengthened with CFRP laminates. Eng Struct 2015;86:213–24.

[41] Dai JG, Gao WY, Teng JG. Bond-slip model for FRP laminates externally bonded to concrete at elevated temperature. J Compos Constr 2013;17(2):217–28.

[42] Michels J, Widmann R, Czaderski C, Allahvirdizadeh R, Motavalli M. Glass transition evaluation of commercially available epoxy resins used for civil engineering applications. Compos B Eng 2015;77:484–93.

[43] Biscaia HC. The influence of temperature variations on adhesively bonded structures: A non-linear theoretical perspective. Int J Non-Linear Mech. 2019;113:67–85.

967 [44] Heshmati M, Haghani R, Al-Emrani M. Environmental durability of adhesively bonded FRP/steel
968 joints in civil engineering applications: State of the art. Compos B Eng 2015;81:259–75.
969 [45] Bai YL, Yan ZW, Ozbakkaloglu T, Gao WY, Zeng JJ. Mechanical behavior of large-rupture-strain
970 (LRS) polyethylene naphthalene fiber bundles at different strain rates and temperatures. Constr
971 Build Mater 2021;297:123786.
972 [46] Gao WY, Teng JG, Dai JG. Effect of temperature variation on the full-range behavior of FRP-to-
973 Concrete bonded joints. J Compos Constr 2012;16:671–83.
974 [47] Gao WY, Dai JG, Teng JG. Analysis of Mode II debonding behavior of fiber-reinforced polymer-
975 to-substrate bonded joints subjected to combined thermal and mechanical loading. Eng Fract Mech
976 2015;136:241–64.
977 [48] Guo D, Gao WY, Dai JG. Effects of temperature variation on intermediate crack-induced
978 debonding and stress intensity factor in FRP-retrofitted cracked steel beams: An analytical study.
979 Compos Struct 2022;279:114776.
980 [49] Guo D, Gao WY, Fernando D, Dai JG. Effect of temperature variation on the plate-end debonding
981 of FRP-strengthened beams: A theoretical study. Adv Struct Eng 2022;25(2):290–305.
982 [50] Guo D, Zhou H, Wang HP, Dai JG. Effect of temperature variation on the plate-end debonding of
983 FRP-strengthened steel beams: coupled mixed-mode cohesive zone modeling. Eng Fract Mech
984 2022;270:108583.
985 [51] Jia DG, Gao WY, Duan DX, Yang J, Dai JG. Full-range behavior of FRP-to-concrete bonded joints
986 subjected to combined effects of loading and temperature variation. Eng Fract Mech
987 2021;254:107928.
988 [52] Firmo JP, Correia JR, Pitta D, Tiago C, Arruda MRT. Experimental characterization of the bond
989 between externally bonded reinforcement (EBR) CFRP strips and concrete at elevated temperatures.
990 Cem Concr Compos 2015;60:44–54.
991 [53] ASTM A370-17. Standard test methods and definitions for mechanical testing of steel products.
992 West Conshohocken, Philadelphia (PA): ASTM International, 2017.
993 [54] ASTM D3039-14. Standard test method for tensile properties of polymer matrix composite
994 materials. West Conshohocken, Philadelphia (PA): ASTM International, 2017.
995 [55] ISO-11359. Plastics-thermomechanical analysis (TMA)-part 2: determination of coefficient of
996 linear thermal expansion and glass transition temperature. International Standard Switzerland, 1999.
997 [56] ASTM-D7028. Standard test method for glass transition temperature (DMA Tg) of polymer matrix
998 composites by dynamic mechanical analysis (DMA). West Conshohocken, Philadelphia (PA):
999 ASTM International, 2017.
1000 [57] Deng S, Hou M, Ye L. Temperature-dependent elastic moduli of epoxies measured by DMA and
1001 their correlations to mechanical testing data. Polymer testing. 2007;26:803-13.
1002 [58] Fernando D, Teng JG, Yu T, Zhao XL. Preparation and characterization of steel surfaces for
1003 adhesive bonding. J Compos Constr 2013;17(6):04013012.
1004 [59] Amada S, Satoh A. Fractal analysis of surfaces roughened by grit blasting. J Adhes Sci Technol
1005 2000;14:27–41.
1006 [60] Deng J, Lee MMK. Behaviour under static loading of metallic beams reinforced with a bonded
1007 CFRP plate. Compos Struct 2007;78:232–42.
1008 [61] Colombi P, Fava G, Sonzogni L. Fatigue crack growth in CFRP-strengthened steel plates. Compos
1009 B Eng 2015;72:87–96.
1010 [62] Fu B, Teng JG, Chen GM, Chen JF, Guo YC. Effect of load distribution on IC debonding in FRP-
1011 strengthened RC beams: Full-scale experiments. Compos Struct 2018;188:483–96.
1012 [63] Barris C, Correia L, Sena-Cruz J. Experimental study on the bond behaviour of a transversely
1013 compressed mechanical anchorage system for externally bonded reinforcement. Compos Struct
1014 2018;200:217–28.

[64] Alexander JGS, Cheng JJR. Shear strengthening of small scale concrete beams with carbon fibre reinforced plastic sheets. Proceedings of the 1st Structural Speciality Conference, Edmonton, Alberta, Canada, 1996; pp. 167–77.

[65] Biscaia HC, Chastre C, Viegas A, Franco N. Numerical modelling of the effects of elevated service temperatures on the debonding process of FRP-to-concrete bonded joints. Compos B Eng 2015;70:64–79.

[66] Smith ST, Teng JG. Interfacial stresses in plated beams. Eng Struct 2001;23:857–71.

[67] Wang JL. Cohesive zone model of intermediate crack-induced debonding of FRP-plated concrete beam. Int J Solids Struct 2006;43:6630–48.

[68] L. De Lorenzis, D. Fernando, J.G. Teng. Coupled mixed-mode cohesive zone modeling of interfacial debonding in simply supported plated beams, International Journal of Solids and Structures 50(14-15) (2013) 2477-2494.

[69] Calabrese AS, D'Antino T, Colombi P, Poggi C. Study on the influence of interface normal stresses on the bond behavior of FRCM composites using direct shear and modified beam tests. Constr Build Mater 2020;262:120029.

[70] Dai JG, Gao WY, Teng JG. Finite element modeling of insulated FRP-strengthened RC beams exposed to fire. J Compos Constr 2015;19:04014046.

[71] Gao WY, Dai JG, Teng JG. Fire resistance design of un-protected FRP-strengthened RC beams. Mater Struct 2016;49:5357–71.

[72] Gao WY, Dai JG, Teng JG. Simple method for predicting temperatures in insulated, FRP-strengthened RC members exposed to a standard fire. J Compos Constr 2015;19:04015013.

[73] Gao WY, Dai JG, Teng JG. Three-level fire resistance design of FRP-strengthened RC beams. J Compos Constr 2018;22:05018001.

[74] Zhao Z, Zhang H, Xian L, Liu H. Tensile strength of Q345 steel with random pitting corrosion based on numerical analysis. Thin-Walled Struct 2020;148:106579.

[75] Yao Y, Yang Y, He Z, Wang Y. Experimental study on generalized constitutive model of hull structural plate with multi-parameter pitting corrosion. Ocean Eng 2018;170:407–15.

[76] Byfield MP, Davies JM, Dhanalakshmi M. Calculation of the strain hardening behaviour of steel structures based on mill tests. J Constr Steel Res 2005;61:133–50.

[77] Liu P, Zhang B, Zheng J. Finite element analysis of plastic collapse and crack behavior of steel pressure vessels and piping using XFEM. J Fail Anal Prev 2012;12:707–18.

[78] Okodi A, Lin M, Yoosef-Ghodsi N, Kainat M, Hassanien S, Adeeb S. Crack propagation and burst pressure of longitudinally cracked pipelines using extended finite element method. Int J Press Vessel Pip 2020;184:104115.

[79] Paredes M, Wierzbicki T, Zelenak P. Prediction of crack initiation and propagation in X70 pipeline steels. Eng Fract Mech 2016;168:92–111.

[80] Ameli I, Asgarian B, Lin M, Agbo S, Cheng R, Duan D-m, Adeeb S. Estimation of the CTOD-crack growth curves in SENT specimens using the extended finite element method. Int J Press Vessel Pip 2019;169:16–25.

[81] Lin M, Agbo S, Duan DM, Cheng JR, Adeeb S. Simulation of crack propagation in API 5L X52 pressurized pipes using XFEM-based cohesive segment approach. J Pipeline Syst Eng Pract 2020;11:04020009.

[82] Agbo S, Imanpour A, Li Y, Kainat M, Yoosef-Ghodsi N, Cheng J, Adeeb S. Development of a tensile strain capacity predictive model for API X42 welded vintage pipelines. J Press Vessel Technol 2020;142(6):061506.

[83] Schiavone A, Abeygunawardana-Arachchige G, Silberschmidt VV. Crack initiation and propagation in ductile specimens with notches: experimental and numerical study. Acta Mech 2016;227:203–15.

[84] Shahzamanian MM, lin M, Kainat M, Yoosef-Ghodsi N, Adeeb S. Systematic literature review of the application of extended finite element method in failure prediction of pipelines. J Pipeline Sci Eng 2021;1(2):241–51.

[85] Rokilan M, Mahendran M. Sub-zero temperature mechanical properties of cold-rolled steel sheets. Thin-Walled Struct 2020;154:106842.